Investigation of New Nonlinear Materials Towards a Stable, Highly Squeezed Light Source

Michael S. Stefszky

A thesis submitted for the degree of
Bachelor of Science with Honours in Physics of
The Australian National University

October, 2007

Declaration

This thesis is an account of research undertaken between February 2007 and October 2007 at The Department of Physics, Faculty of Science, The Australian National University, Canberra, Australia.

Except where acknowledged in the customary manner, the material presented in this thesis is, to the best of my knowledge, original and has not been submitted in whole or part for a degree in any university.

Michael S. Stefszky
October, 2007

Acknowledgements

This year has been amazing! Honours year has been a terrific experience and even though the hours worked have been plentiful, I have enjoyed just about every one of them.

Firstly, thankyou to Ping Koy Lam and Thomas Symul for inviting me to join in the quantum optics group. At the end of last year I had originally decided that it was time for a break from all the study, but now I am very glad that I had the chance to continue my study and complete my honours. The other three years of university pale in comparison to my honours year, in just about all aspects. Thankyou to Ping Koy for giving me, and all of your students, the best possible chance of reaching our full potentials, your willingness to aid in any way you can never went unnoticed.

Thankyou to everyone in the office, past and present, for providing such a great environment to come to every day over the last year, for the warm smiles and for the conversations that woke me up when I thought that my head was about to crash into my computer.

Thanks also go out to Neil and Shane from the electronics workshop, for their conversations which helped illuminate much of the electrical workings of the experiment and for constructing the HV amps and PID's in the experiment. Thanks also go to Hans Bachor for allowing Neil time to get on top of my order. Also to the guys in the mechanical workshop for your help, and for the pride you take in your work, of which the bow-tie cavity used in the experiment is testament to.

To my family for their support, thankyou. Thankyou also for the dinners which were ready for me when I got home, and supporting me in other ways. To Warren for giving me somebody to enjoy my other hobbies with, to keep me sane.

To the other honours students, especially Sean, Sheon and Jeff. Thankyou for your friendship and reminding me that problems with experimental physics were not limited to just my optics table.

A big thanks also to Nicolai, Thomas, Assad, Ben, Kirk, Ping Koy and Phil for either reading through my thesis for me or always being available and happy to answer any and all questions that I managed to come up with. Your help was appreciated.

Thankyou ever so much to both Nicolai and Assad, sharing the optics bench with you was one of the highlights of this year. Nicolai, your brilliance is matched only by your humility. I cannot thank you enough for the help you have given me this year, from answering every question I could fathom, to somehow making being in the lab late at night not such a chore. Your presence and experience is going to be missed sorely, by myself and everyone else in the group. Thankyou to Assad for your amazing attitude towards your work and life in general. Your positive attitude is a true inspiration. I sincerely wish the both of you, along with everybody else I have had the opportunity to spend time with this year, the best for the future in all aspects of your lives.

Finally, a mention must be made for the music which helped to keep me awake during late nights of thesis writing and gave me something to look forward to on the drive home from university. Iron Maiden, Judas Priest, Helloween, Nightwish and Vanishing Point to name a few, you guys rock and I look forward to seeing at least two of you next year.

Abstract

Useful applications for squeezed states of light have been theorized for decades, however, only recently have advancements in the technology allowed for experimental investigations into applications of squeezed light. Most experiments which involve squeezing could be benefited by having a squeezing source which produces stable, highly squeezed states.

This thesis investigates the generation of squeezed states of light which exhibit these properties, stability and high levels of squeezing. The key investigations are;

- Initially a model is produced which estimates the expected level of squeezing in a singly or doubly resonant cavity. The properties of the cavity are altered by varying the reflectivity of one of the cavity mirrors for either the pump or seed frequencies. The effects of increasing pump power and introducing additional losses into the cavity are investigated as well as the optimum resonance conditions for maximum squeezing.

- Built 3 squeezers with 3 different nonlinear mediums. A maximum squeezing value was found for each of the crystals and any effects which degraded or improved the results were investigated.

  Using PPKTP 5.8±0.1dB of squeezing was directly observed.

  Using PPSLT 4.9±0.1dB of squeezing was directly observed. PPSLT was found to have an unusually high threshold power, indicating that the crystal may have had a nonlinear coefficient much lower than expected.

  Using 1.7% MgO:PPSLN 1.1±0.2dB of squeezing was observed. The poor squeezing results were due to an anomaly in the material which affected its reflectivity and is investigated in the thesis.

- The intra-cavity loss introduced to the system through the addition of each of the crystals was inferred from measurements of the cavity finesse, and the effect of this loss is explored.

- Demonstrated the usefulness of a wedge in periodically poled materials to reach the optimum resonance condition in the squeezing setup. It is shown that the wedge is capable of cancelling the dispersion introduced in a round trip of the cavity, with no discernible negative effects.

These investigations are used to comment on the suitability of each of these crystals for future experiments involving squeezing and possible modifications to improve the results.

Contents

List of Figures

List of Tables

Summary of symbols and acronyms

Term	Definition
$\vec{B}$	Magnetic flux density
$\vec{E}$	Electric field
$\vec{D}$	Electric flux density
$\vec{H}$	Magnetic field
$\vec{A}$	Vector potential in Coulomb gauge (with condition $\nabla.\vec{A} = 0$)
$\vec{P}$	Electric Polarization Density
$\chi^{(2)}$	Second order nonlinearity coefficient or second order susceptibility
μ_0	Magnetic Permeability
ε_0	Electric Permittivity
c	Speed of light in a vacuum
$\hat{a}, (\hat{a}^\dagger)$	Annihilation and (creation) operators of fundamental cavity mode
$\hat{A}, (\hat{A}^\dagger)$	Annihilation and (creation) operators of fundamental travelling wave
$\hat{X}^+, (\hat{X}^-)$	Amplitude and (phase) quadrature operators
$\hat{X}^\theta$	General quadrature operator
$\langle h \rangle$	Expectation value of function h
α	Classical cavity mode amplitude
$\delta\hat{a}, (\delta\hat{a}^\dagger)$	First order fluctuating part of annihilation and (creation) operators
Δ	Standard deviation, square root of variance Δ^2
$\hat{n}$	Photon number operator
QNL	Quantum Noise Limit, used interchangeably with shot noise limit (SNL)
ω	Optical frequency
DOPA	Degenerate Optical Parametric Amplifier
OPO	Optical Parametric Oscillator
NDOPA	Non-Degenerate Optical Parametric Amplifier
δ	Frequency shift about a given frequency ω
Δ	In nonlinear optics denotes frequency shifts about ω for all possible Δ
$\chi, (\chi^{(3)})$	Linear and (third order) susceptibility
SHG	Second harmonic generation
SFG	Sum frequency generation
THG	Third harmonic generation
L_c	Coherence length
Δk	Phase mismatch
$I_F, (I_{SH})$	Intensity of fundamental and (second harmonic) fields
PM, (QPM)	Phase matching and (quasi-phase matching)

Term	Definition
MgO:PPSLN	Magnesium oxide doped periodically poled stoichiometric lithium niobate
PPSLT	Periodically poled stoichiometric lithium tantalate
PPKTP	Periodically poled potassium titanyl phosphate
$\hat{a}, \hat{b}$	Annihilation operators for fundamental and (second harmonic) cavity modes
$\hat{A}, \hat{B}$	Annihilation operators for fundamental and (second harmonic) travelling waves
$\Delta_a, (\Delta_b)$	Fundamental and (second harmonic) frequency mismatches
$\kappa_a, (\kappa_b)$	Fundamental and (second harmonic) total decay rate of cavity
τ	Cavity round trip time
ϵ	Nonlinear coupling coefficient
$\kappa^a_{in}, (\kappa^b_{in})$	Fundamental and (second harmonic) coupling rates for input mirror
$\kappa^a_{out}, (\kappa^b_{out})$	Fundamental and (second harmonic) coupling rates for output mirror
$\kappa^a_l, (\kappa^b_l)$	Fundamental and (second harmonic) coupling rates for cavity loss
$\delta\hat{X}^+_a, (\delta\hat{X}^+_b)$	Fundamental and (second harmonic) fluctuations in the amplitude quadrature
$\delta\tilde{\hat{X}}^+_a, (\delta\tilde{\hat{X}}^+_b)$	Fundamental and (second harmonic) amplitude fluctuations in frequency domain
V_{Aout}	Amplitude quadrature output variance of fundamental mode
η_{esc}	Escape efficiency at fundamental frequency
$R_a, (R_b)$	Reflectivities of input/output coupler for fundamental and (pump)
PDH	Pound-Drever-Hall locking technique
PZT	Piezo-electric transducer
PID	Proportional-integral-differentiator
ν	Homodyne visiblity
$\mathfrak{F}$	Cavity finesse
FSR	Free spectral range
FWHM	Full width at half maximum or linewidth of cavity response

Introduction

Squeezed states of light are states of light for which the uncertainty of one of the quadratures, amplitude or phase, is below the quantum noise limit (QNL). This is directly related to the Heisenberg Uncertainty Principle from quantum mechanics. As is found for the momentum and position operators of a particle, the phase and amplitude quadrature operators do not commute, and hence there is a minimum uncertainty between the two observables. We can however, through non-linear interactions, create a state of light for which the uncertainty of one of these observables, or quadratures, is below the QNL. This is done at the cost of adding noise to the other quadrature in order to preserve the Heisenberg Uncertainty Principle. This is what is known as a squeezed state of light.

The properties of squeezed states of light allow for improvement of many current processes which rely upon laser light and also allow for many new fields of research . Any measurement in which only one of the quadratures is probed can be enhanced with the use of squeezed light. For example, a squeezed state of light which has reduced noise in the phase quadrature can improve the sensitivity of gravitational wave detectors that are based on a Michelson interferometer. In such a design, a disturbance in one arm will affect the fringe patterns seen at the output, due to an acquired difference between the phase of the two arms as they travel separate paths. The amplitude of the light ideally does not affect the measurement. Gravitational wave detection is a field of physics which is chasing accuracies we have never before seen and the use of squeezed light in such setups is almost an inevitability [1]. Another example of a current process which may be improved by squeezing is optical imaging. With the use of squeezed light it is possible to construct a light mode which has strong spatial correlations, allowing for enhanced accuracy in beam displacement measurements as experimentally observed by Treps [2]. Finally, other properties of this state of light such as fragility, can be utilized for current research fields such as quantum cryptography [3].

One method of creating squeezing is to use an Optical Parametric Amplifier (OPA) or an Optical Parametric Oscillator (OPO). An OPO or an OPA is essentially an optical cavity with a non-linear material at the focus. Depending on the setup, one or more fields are directed into the cavity, where the fields build up and will undergo a nonlinear interaction within the crystal . One of the major limiting factors in creating squeezed states with an OPA or an OPO, is the strength of the coupling between the light fields involved. Many crystals have been found that possess the required properties to achieve high levels of squeezing, though certainly none of them are ideal.

The strength of the second order nonlinearity, given by the $\chi^{(2)}$ coefficient of a material, is stronger in some directions through the crystal than others. The higher this value is in the experiment, the more squeezing we could expect at the output. As is often the case, enhancing the system for one parameter will introduce unwanted effects, or affect

the performance of other system parameters. The unwanted effect gained by using the direction in the crystal with the highest $\chi^{(2)}$ value, is often an inability to achieve a condition known as phase matching. The phase matching ensures momentum conservation in the squeezing process. Without accurate phase matching, only low levels of squeezing are possible, if at all. One method to circumvent this problem is to use quasi-phase matching

The technique of quasi-phase matching was first theorized in 1962 [4] but the most common quasi-phase matching technique used nowadays, *electric field periodic poling*, was developed in 1993 [5, 6]. This method uses an array of electrodes to change the spontaneous polarization domains within the crystal. Quasi-phase matching allows for directions in the crystals with higher $\chi^{(2)}$ values to be used where normal phase matching is not possible. By changing the sign of the nonlinearity coefficient at specific intervals in the crystal, we can stop the nonlinear process from reversing at certain points within the crystal.

This thesis purports to explore a number of new and improved non-linear materials, *Magnesium Oxide Doped Periodically Poled Stoichiometric Lithium Niobate* (MgO:PPSLN), *Periodically Poled Stoichiometric Lithium Tantalate* (PPSLT) and *Periodically Poled Potassium Titanyl Phosphate* (PPKTP). As indicated, all of these materials have undergone periodic poling, so that the optimum direction in the crystal might be utilized. While current periodic poling techniques do allow for increased $\chi^{(2)}$ values in experiments, imperfections in current methods mean that there are still higher values to be obtained. Also of interest is that two of these crystals are stoichiometric, implying that there are less intrinsic defects in the crystal structure, which in turn should increase the energy threshold for which irreversible damage is done to the crystal. By having a higher damage threshold, one is able to increase the optical power in the system, which may then allow for higher levels of squeezing.

The aim of the experiment will be to obtain stable, high levels of squeezing. In doing so, we will be comparing the performance of the different non-linear crystals, so that the current optimum non-linear material for this process might be found. Much debate is formed over which nonlinear crystal will be the most suitable in future experiments to reliably produce high levels of squeezing. This thesis hopes to explore the pros and cons of each material.

To achieve these aims, an OPO will be constructed using a newly designed "bow-tie" cavity setup. The advantages to this type of cavity are that there are many options for entering and extracting the light from the cavity, as well as the ability to replace the non-linear crystal inside the cavity with only minor modifications to the experimental setup. This will allow for the comparison of the different non-linear crystals in almost identical environments.

Quantum theory of light

2.1 A quantum description of light

The following chapter introduces the key concepts for experimentation in quantum optics. The electromagnetic field is first quantized, and through this quantization we are introduced to the annihilation and creation operators as a means of describing the light field. The quadrature operators and the number operator are then introduced and their role in describing various states of light is explored.

2.1.1 Quantising the electromagnetic field

Many introductions to the quantum mechanical nature of light seem to begin by defining the amplitude and phase quadrature operators and then introducing their relationship to the Heisenberg uncertainty principle. Here we will take a more detailed approach and give an overview on the quantization of the electromagnetic field. We follow the same method as that found in Walls and Milburn [7].

The first step is to examine the source-free Maxwell's equations

$$\nabla.\vec{B} = 0 \tag{2.1}$$

$$\nabla \times \vec{E} = -\frac{\partial \vec{B}}{\partial t} \tag{2.2}$$

$$\nabla.\vec{D} = 0 \tag{2.3}$$

$$\nabla \times \vec{H} = \frac{\partial \vec{D}}{\partial t} \tag{2.4}$$

Where $\vec{B} = \mu_0 \vec{H}$, $\vec{D} = \varepsilon_0 \vec{E} + \vec{P}$ and μ_0 is the magnetic permeability, ϵ_0 is the electric permittivity and we have the identity that $\mu_0 \varepsilon_0 = \frac{1}{c^2}$. $\vec{E}$ is the electric field, $\vec{D}$ is the electric flux density, $\vec{P}$ is the electric polarization density, $\vec{H}$ is the magnetic field and $\vec{B}$ is the magnetic flux density.

We now use the fact that Maxwell's equations are gauge invariant to move to the Coulomb gauge, with the constraint that

$$\nabla.\vec{A} = 0 \tag{2.5}$$

where $\vec{A}(\vec{r}, t)$ is a vector potential. In this gauge we can rewrite the magnetic and electric fields as

$$\vec{B} = \nabla \times \vec{A} \tag{2.6}$$

$$\vec{E} = -\frac{\partial \vec{A}}{\partial t} \tag{2.7}$$

Starting from 2.4 and making use of equations 2.6 and 2.7 and the vector identity $\nabla \times \nabla \times \vec{A} = \nabla(\nabla.\vec{A}) - \nabla^2\vec{A}$ we arrive at the wave equation for the vector potential $\vec{A}(\vec{r},t)$,

$$\nabla^2\vec{A}(\vec{r},t) = \frac{1}{c^2}\frac{\partial^2\vec{A}(\vec{r},t)}{\partial t^2} \tag{2.8}$$

The next step is to separate the vector potential $\vec{A}(\vec{r},t)$ into two complex terms given by

$$\vec{A}(\vec{r},t) = \vec{A}^+(\vec{r},t) + \vec{A}^-(\vec{r},t) \tag{2.9}$$

where $\vec{A}^+(\vec{r},t)$ contains the terms which vary as $e^{-i\omega t}$ for $\omega > 0$ and likewise, $\vec{A}^-(\vec{r},t)$ will contain the terms which vary as $e^{i\omega t}$ for $\omega > 0$.

In order to quantize the field we now restrict the problem to a confined volume, much in the same way as is done for the quantum harmonic oscillator. This allows us to expand the vector potential in terms of vector mode functions and Fourier coefficients, resulting in

$$A^{(+)}(\vec{r},t) = \sum_k c_k\vec{u}_k(\vec{r})e^{-i\omega_k t} \tag{2.10}$$

Where c_k are the Fourier coefficients, which will be constant for a free field and the $\vec{u}_k$ are the vector mode functions for a given frequency. The sum over k is used to represent that the total electric field is made up of the sum of all fields at all frequencies k. Comparing this form of the vector potential with the previous wave equation for the vector potential, equation 2.8, and the condition for the Coulomb gauge, equation 2.5, we find that the vector mode functions must satisfy,

$$(\nabla^2 + \frac{\omega_k^2}{c^2})\vec{u}_k(\vec{r}) = 0 \tag{2.11}$$

$$\nabla.\vec{u}_k(\vec{r}) = 0 \tag{2.12}$$

Using equation 2.9 and equation 2.7 it is possible to now quantize the electromagnetic field. In order to transform these classical equations into their quantum analogues, the requirement is that the c_k are replaced with suitable operators,

$$\vec{E}(\vec{r},t) = i\sum_k(\frac{\hbar\omega_k}{2\varepsilon_0})^{\frac{1}{2}}[\hat{a}_k\vec{u}_k(\vec{r})e^{-i\omega_k t} - \hat{a}^\dagger\vec{u}_k^*(\vec{r})e^{i\omega_k t}] \tag{2.13}$$

The operators, a_k and $a_k^\dagger$ are dimensionless and are the crux of the quantization. They are required to be mutually adjoint operators and owing to the boson nature of photons we require that they fulfill the boson commutation relations.

$$[\hat{a}_k, \hat{a}_{k'}] = \left[\hat{a}_k^\dagger, \hat{a}_{k'}^\dagger\right] = 0 \tag{2.14}$$

$$\left[\hat{a}_k, \hat{a}_{k'}^\dagger\right] = \delta_{kk'} \tag{2.15}$$

The annihilation, a_k, and creation, $a_k^\dagger$, operators fulfill these requirements and as such are chosen to represent the electromagnetic field.

To summarise, we have first chosen the Coulomb gauge, restricted the field to a given volume, written the vector potential in terms of vector mode functions and have finally

chosen the annihilation and creation operators to take the place of the resulting dimensionless coefficients. From this point on we will drop the k subscript, which defines the mode of the field under question and assume that we are looking only at a single mode unless otherwise specified.

2.1.2 Quadrature operators

Now that the light field has been quantized and that the annihilation and creation operators have been introduced, it is time to define the phase and amplitude quadrature operators. The annihilation and creation operators are non-Hermitian, this means that they cannot be observed in the lab. In order to carry out verifiable experiments we will be required to introduce Hermitian operators. The two which are most commonly probed are the amplitude and phase quadrature operators. There are many ways to introduce these operators, but keeping with the previous derivations, one way to introduce them is to write the non-Hermitian annihilation operator in terms of two Hermitian operators. We write

$$\hat{a} = \frac{\hat{X}^+ + i\hat{X}^-}{2} \tag{2.16}$$

where the amplitude quadrature operator, $\hat{X}^+$, and the phase quadrature operator, $\hat{X}^-$, are the real and imaginary part of the complex amplitude of the annihilation operator respectively. We can also represent the amplitude and phase quadrature operators in terms of the annihilation and creation operators as

$$\hat{X}^+ = \hat{a} + \hat{a}^\dagger \tag{2.17}$$

$$\hat{X}^- = i(\hat{a}^\dagger - \hat{a}) \tag{2.18}$$

These operator can also be written in a different through the use of another operator, known as the general quadrature operator,

$$\hat{X}^\theta = \hat{a}e^{-i\theta} + \hat{a}^\dagger e^{i\theta} \tag{2.19}$$

of which the amplitude and phase quadrature operators are special cases. Namely, for $\theta = 0$ we find the amplitude quadrature operator and for $\theta = \frac{\pi}{2}$ we return the phase quadrature operator. When producing squeezed states the squeezing may lie on any angle theta relative to a local oscillator, and hence the general quadrature operator may be used to probe the properties of this rotated state of light.

From here we can now look at what effect the Heisenberg uncertainty principle will have on the amplitude and phase quadrature operators. We know that the principle applies to any two non-commuting operators. The commutation relation between any two Hermitian operators, $\hat{A}$ and $\hat{B}$, is given by

$$[\hat{A}, \hat{B}] = \hat{A}\hat{B} - \hat{B}\hat{A} \tag{2.20}$$

By definition, for these operators to commute implies that their commutation relation is equal to zero. If they do not commute then the Heisenberg uncertainty principle tells us that there is a limit to the precision that we can simultaneously measure both these properties, given by

$$\Delta\hat{A}\Delta\hat{B} \geq \frac{1}{2i}\langle[\hat{A}, \hat{B}]\rangle \tag{2.21}$$

Where $\Delta\hat{A}$ is the standard deviation in the observable $\hat{A}$ and likewise for $\hat{B}$. $\langle[\hat{A},\hat{B}]\rangle$ denotes the expectation value of the commutation relation of the Hermitian operators $\hat{A}$ and $\hat{B}$. Calculating the commutation relation for the amplitude and phase quadrature operators, and simplifying using the boson commutation relations, equations 2.14 and 2.15, yields

$$[\hat{X}^+,\hat{X}^-]=2i \tag{2.22}$$

Placing this into the general form of the Heisenberg uncertainty principle will result in the uncertainty relation for the two quadrature operators, given by

$$\Delta\hat{X}^+\Delta\hat{X}^-\geq 1 \tag{2.23}$$

This principle places a bound on how well we can simultaneously know both the phase and amplitude of a mode of light.

2.1.3 Linearising the operators

Linearisation of the annihilation operator was first explored by Yurke in 1984 [8]. Linearising the annihilation operator allows for the analytical solving of many quantum optics problems. We write the annihilation operator as a classical coherent amplitude term plus a first order fluctuating term, which is still a time varying operator.

$$\hat{a}(t)=\alpha+\delta\hat{a}(t) \tag{2.24}$$

And likewise for the creation operator,

$$\hat{a}^\dagger(t)=\alpha^*+\delta\hat{a}^\dagger(t) \tag{2.25}$$

Where α, the coherent classical amplitude, is the expectation value of the annihilation operator, $\langle a\rangle$, and $\delta\hat{a}(t)$ is the first order fluctuating term. The linearisation operation relies on the average of the fluctuating terms being zero and the coherent amplitude of the state of light being much larger than the first order fluctuating term

$$<\delta\hat{a}(t)>=<\delta\hat{a}^\dagger(t)>=0 \tag{2.26}$$

$$|\,\delta\hat{a}(t)\,|\ll|\,\alpha\,| \tag{2.27}$$

Now we explore the variance of the quadrature operators. We begin by defining the variance, Δ^2, of some operator $\hat{A}$,

$$\Delta^2(\hat{A})=(\Delta(\hat{A}))^2=<\hat{A}^2>-<\hat{A}>^2 \tag{2.28}$$

and then explicitly place the linearisation into this definition and simplify to find for the amplitude quadrature that

$$\begin{aligned}\Delta^2(\hat{X}^+) &= <(\hat{X}^+)^2>-<\hat{X}^+>^2\\ &= <(\hat{a}+\hat{a}^\dagger)^2>-<\hat{a}+\hat{a}^\dagger>^2\\ &= <(\alpha+\delta\hat{a}+\alpha^*+\delta\hat{a}^\dagger)^2>-<\alpha+\delta\hat{a}+\alpha^*+\delta\hat{a}^\dagger>^2\\ &= <(\delta\hat{a}+\delta\hat{a}^\dagger)^2>\\ &= <(\delta\hat{X}^+)^2>\end{aligned} \tag{2.29}$$

and similarly for the phase quadrature operator we find

$$\begin{aligned}\Delta^2(\hat{X}^-) &= <(\hat{X}^-)^2> - <\hat{X}^->^2 \\ &= <(i(\delta\hat{a}^\dagger - \delta\hat{a}))^2> \\ &= <(\delta\hat{X}^+)^2> \end{aligned} \tag{2.30}$$

The linearization of the operators is a powerful technique which greatly simplifies calculations and allows for analytical solutions to many quantum optics problems.

2.1.4 The number operator

The number operator can be written

$$\hat{n} = \hat{a}^\dagger\hat{a} \tag{2.31}$$

and when acting upon a state, returns the average number of photons in the state. As with the quadrature operators, we can linearize the number operator, this time assuming that α is real we find,

$$\begin{aligned}\hat{n} &= \hat{a}^\dagger\hat{a} \\ &= (\alpha^* + \delta\hat{a}^\dagger)(\alpha + \delta\hat{a}) \\ &= \alpha^2 + \alpha(\delta\hat{a} + \delta\hat{a}^\dagger) + \delta\hat{a}^\dagger\delta\hat{a} \qquad (2.32) \\ &\approx \alpha^2 + \alpha(\delta\hat{X}^+) \qquad (2.33)\end{aligned}$$

where we have removed the second order fluctuation term on the assumption that it will have little effect to the overall result. This assumption is true for large photon numbers, as is explored in [9].

2.2 Representations of different states of light

2.2.1 The vacuum state

The vacuum state, $\mid 0 >$ is arguably the defining difference between classical optics and quantum optics. As with many quantum effects, there is no analogue in classical mechanics. The number operator applied to the vacuum state results in

$$< 0 \mid \hat{n} \mid 0 >= 0 \tag{2.34}$$

indicating that there are no photons in the vacuum state. However, this does not imply that the vacuum state is free from fluctuations. What one actually finds is

$$\langle 0|\Delta^2\hat{X}^+|0\rangle = \langle 0|\Delta^2\hat{X}^-|0\rangle = 1 \tag{2.35}$$

The uncertainty in both quadratures is equal and is exactly the minimum uncertainty allowed by the Heisenberg uncertainty principle. Due to this, the vacuum state is said to be a minimum uncertainty state. This simple result captures the heart of many quantum optics experiments. Empty space is not quite empty, it contains fluctuations in the electric field which play a very important part in any quantum optics experiment.

2.2.2 The coherent state

The coherent state of light, $\mid \alpha >$ is that which most closely approximates the classical notion of light, in the sense that it is a bright beam with the minimum fluctuations allowed by the Heisenberg uncertainty principle. It, like the vacuum state, has the property that

$$\Delta^2 \hat{X}^+ = \Delta^2 \hat{X}^- = 1 \tag{2.36}$$

and as such is also a minimum uncertainty state. The difference between the coherent state and the vacuum state is that the coherent state has photons in it, whereas the vacuum state does not. This means that the value of α for a coherent state is nonzero.

The coherent state can be mathematically achieved through the use of the displacement operator

$$\hat{D}(\alpha) = e^{(\alpha \hat{a}^\dagger - \alpha^* \hat{a})} \tag{2.37}$$

and utilizing this operator we may transform a vacuum state to a coherent state

$$\hat{D}(\alpha) \mid 0 >= \mid \alpha > \tag{2.38}$$

2.2.3 The squeezed state

A squeezed state of light has the property that the variance in one of its quadratures is less than unity. Such an operation is not without consequence. The Heisenberg uncertainty principle necessitates that the variance in the other quadrature increases, such that the inequality

$$\Delta^2 \hat{X}^+ \Delta^2 \hat{X}^- \geq 1 \tag{2.39}$$

still holds. Mathematically, we can generate an arbitrary squeezed state through the use of the squeeze operator and the displacement operator. The squeeze operator $\hat{S}(\rho)$, is defined as

$$\hat{S}(\rho) = e^{\frac{1}{2}(\rho^* \hat{a}^2 - \rho \hat{a}^{\dagger 2})} \tag{2.40}$$

$$\rho = r e^{i\theta} \tag{2.41}$$

where r is known as the squeeze parameter and satisfies $r \geq 0$. The squeezed state is thus produced from the vacuum state as

$$\hat{D}(\alpha)\hat{S}(\rho) \mid 0 >= \mid \alpha, \rho > \tag{2.42}$$

For an amplitude squeezed state, for which $\theta = 0$, investigation of the properties of this state will yield

$$< \alpha, \rho \mid \hat{a}^\dagger \hat{a} \mid \alpha, \rho > = sinh^2 r + \alpha^2 \tag{2.43}$$

$$\Delta(\hat{X}^+) = e^{-r} \tag{2.44}$$

$$\Delta(\hat{X}^-) = e^{r} \tag{2.45}$$

At this point, provided the meaning is unambiguous, we shall remove the hats from all operators.

2.3 Methods for visualising the states of light

2.3.1 The ball on stick diagram

Here we introduce the ball on stick diagram, which is an intuitive way of representing a state of light, indicating the uncertainties in both quadratures as well as the coherent amplitude of the light. From these plots it is not hard to imagine where the term "squeezed light" arose.

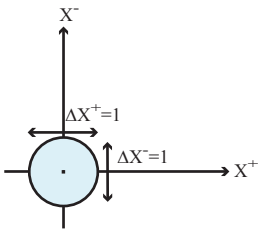

Figure 2.1: Vacuum state ball on stick diagram. The vacuum state is centred on the origin to indicate that the classical coherent amplitude α, is equal to zero. It has a standard deviation equal to unity in both of the quadratures.

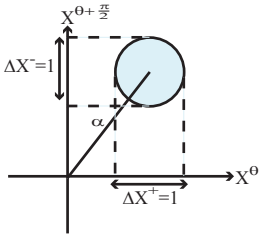

Figure 2.2: Coherent state ball on stick diagram. The coherent state has a stick drawn from the origin to the centre of the ball, indicating the value of α. The standard deviation in each quadrature is equal to unity.

Figure 2.1 depicts a ball on stick diagram of a vacuum state of light. The ball is centered on the origin. This is an indication that the vacuum state does not have a classical coherent amplitude, $\alpha = 0$. The ball represents the fluctuations which lie within one standard deviation of the mean value for the amplitude and phase quadratures. In the classical picture of the electromagnetic field, the ball would not exist and the end of the stick would represent the electromagnetic field with a coherent amplitude and no uncertainty region. The projection of the ball onto the x-axis indicates that the uncertainty, or standard deviation, in the amplitude quadrature is unity, and likewise the projection of the ball onto the y-axis indicates that the uncertainty of this state in the phase quadrature is also one. This is a minimum uncertainty state which means that equation 2.23 is a strict equality. Hence the area of this circle is the minimum allowed by the Heisenberg uncertainty principle. The ball represents the chance of a measurement returning specific properties of the state, given by a two dimensional Gaussian profile. The diameter of the ball shows fluctuations that lie within one standard deviation of the mean value and as such any measurement will have a 64% chance of lying within the ball.

Figure 2.2 shows a ball on stick representation of a coherent state of light. Note that the size of the ball is exactly the same as for the vacuum state. The difference is that this ball is displaced from the origin and the centre of the ball is connected to the origin via a "stick". The length of this stick indicates the magnitude of the classical coherent amplitude of the state, α. As for the vacuum state, the coherent state is a minimum uncertainty state, indicated by having an uncertainty equal to unity in each of the quadratures. In this figure it is now easier to visualise how this representation aids in understanding the fluctuations of the light field. We may think of a measurement of this state as a determination of the position of the end of the stick along one of the quadratures. The fluctuations in the light field, however, will cause this stick to grow, shrink and rotate. The chance of measuring the stick, or state of light, at any given location is given by a two dimensional Gaussian

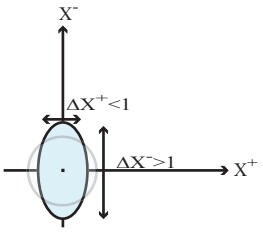

Figure 2.3: Squeezed vacuum state. The squeezed vacuum state is centred on the origin and has a standard deviation less than unity in one of the quadratures.

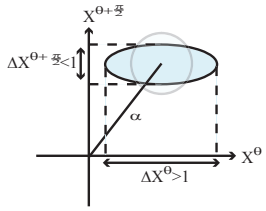

Figure 2.4: Bright squeezed state. The bright squeezed state has a classical coherent amplitude indicated by the length of the stick and has a standard deviation less than unity in one of the quadratures.

centred at the middle of the ball.

Figure 2.4 depicts an amplitude squeezed state in the ball on stick diagram. The ellipse is centred about the origin, indicating that the vacuum state has no coherent amplitude. We note that the amplitude squeezed state, however, has a projection onto the x-axis of less than 1 and a projection onto the y-axis of greater than 1. The fluctuations in the X^θ quadrature have been reduced at the cost of increasing the fluctuations in the othogonal, quadrature in order to preserve the Heisenberg uncertainty principle relationship between the two. A squeezed state need not necessarily be a minimum uncertainty state, equation 2.23 may be a strict inequality, so long as the standard deviation in one of the quadratures is less than 1.

2.3.2 Classical sidebands

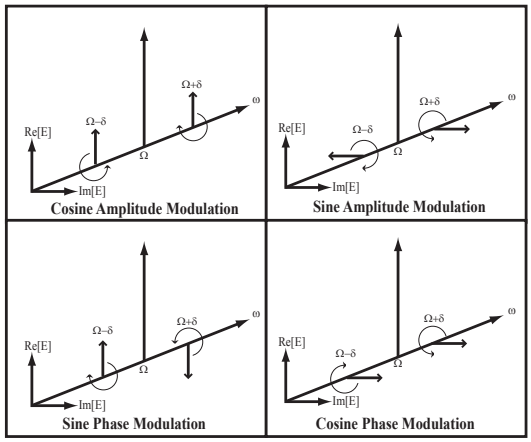

Figure 2.5: Classical modulation sidebands. The carrier at frequency Ω is accompanied by the modulation sidebands at $\Omega + \delta$ and $\Omega - \delta$. The sidebands rotate around the carrier as depicted.

Another method of depicting states of light is through the use of the sideband model. The sideband model for the different states of light is perhaps not as immediately intuitive as the ball on stick model but is better suited to describing the processes involved in squeezing. Here we will assume that the reader is familiar with the basic classical concepts

of modulation. For a more thorough background, the reader is directed to [10]. We begin by first recalling how phase and amplitude modulation appear in the sideband picture.

Figure 2.5 shows four cases of classical modulation in the sideband model. We need only look at the first order sidebands for small modulation depths. With this assumption in place we can then draw both amplitude and phase modulation as a pair of sidebands. In the frame where the carrier is stationary, these sidebands rotate in opposite directions around the carrier, such that for amplitude modulation the sidebands will align in the real axis of the field and for phase modulation the sidebands will align in the imaginary axis of the electric field. The important concept which is highlighted in the sideband model, is that modulation at a frequency δ can be pictured as a correlation between sidebands at $\Omega + \delta$ and $\Omega - \delta$. These sidebands will rotate in opposite directions around the carrier at a frequency δ. In the classical model there are only 3 fields present at three distinct frequencies, the carrier and two sidebands.

2.3.3 Quantum sidebands

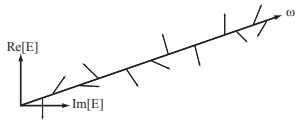

Figure 2.6: Sideband model of the vacuum state. The vacuum state is visualised as "sidebands" that span all of ω and are uncorrelated.

Now we can examine the sideband model of the vacuum state, shown in figure 2.6. We can think of the vacuum fluctuations as a continuum of "sidebands" for all ω with no centre frequency and no correlations between any of these sidebands. These fluctuations will have an average energy equal to $\sqrt{\frac{\hbar\omega_k}{2}}$, this is known as the zero-point energy or vacuum energy and is present at all frequencies ω. It is these sidebands which introduce the quantum noise limit (QNL) on any measurement. The sidebands rotate about the ω axis for all frequencies and represent the vacuum fluctuations across the entire spectrum. A coherent state is represented similarly, but with a large amplitude vector at some frequency, Ω, as shown in figure 2.7. The fluctuations across the entire spectrum are still present.

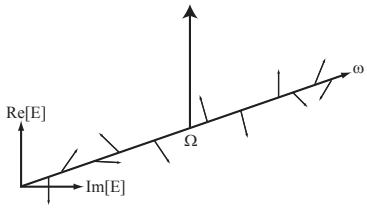

Figure 2.7: Sideband model of the coherent state. A strong carrier field at frequency Ω is accompanied by vacuum fluctuations across the entire spectrum.

Non-linear optics

3.1 Nonlinear optical processes

Nonlinear optical processes, by definition, are those processes for which the output does not depend linearly upon the electric field strength of the input. Nonlinear processes allow for the manipulation of sidebands in ways that linear processes are not capable of, and without such processes, effects such as second harmonic generation and squeezing are not possible. In this chapter we look at the theory behind many nonlinear processes which take place in certain dielectric media and some of the experimental setups we can construct which take advantage of these nonlinear processes.

3.2 The second order non-linearity

We begin by examining the second order optical nonlinear interaction process, a more complete treatment of which can be found in Saleh and Teich [11]. It is this interaction, taking place within our nonlinear medium, which we shall utilize in order to produce the desired squeezed states. In a linear interaction, an electromagnetic wave incident on a dielectric material will generally induce dipole moments in the material. This will in turn produce a polarisation wave, which in a linear medium will have the same frequency as the incident optical electromagnetic wave. This polarisation wave will add to the total electric flux density $\vec{D}$, thus altering the total electric field within the material. This process will continue to repeat itself. For the linear case we can write the electric polarisation density as

$$\vec{P} = \varepsilon_0 \chi \vec{E} \tag{3.1}$$

Where χ is the linear susceptibility of the dielectric medium and is a measure of the polarisation that a given incident electric field will induce. The output of such an interaction will depend linearly upon the electric field strength of the light added, hence the title, a linear interaction.

For low input intensities, the second and third order non-linear interactions will approximately follow this linear process. Increase the intensity of the incident field on a nonlinear medium, however, and a plethora of nonlinear effects may arise. Explicitly stating the induced polarisation, including all of the higher order terms, we may write

$$\vec{P} = \varepsilon_0(\chi \vec{E} + \chi^{(2)}\vec{E}^2 + \chi^{(3)}\vec{E}^3 + \dots) \tag{3.2}$$

Where $\chi^{(2)}$ is the second order nonlinear susceptibility, and $\chi^{(3)}$ is the third order

nonlinear susceptibility. This equation highlights the fact that the polarisation will induce harmonics of the initial incident light field. For an incident plane wave of frequency ω, the second order interaction will produce a plane wave of frequency 2ω and the third order interaction will produce a wave of frequency 3ω. The second order interaction will allow for such processes as second harmonic generation (SHG), sum frequency generation (SFG), optical parametric amplification (OPA) and optical parametric oscillation (OPO). The third order interaction will allow for such processes as the Kerr effect, third harmonic generation (THG) and self focussing. For a second order $\chi^{(2)}$ susceptibility to be non-zero in a medium, we require that the medium lacks symmetry in some direction. Most crystal structures meet this requirement and this is an indication as to why many crystals can be used to generate squeezing by utilizing the second order nonlinearity. Here we will only investigate a selection of these nonlinear processes. A more detailed explanation of many of the other processes may be found in White [12] or Saleh and Teich [11].

3.3 Upconversion processes

Often it is useful to look at nonlinear processes from the view of single photon interactions. An upconversion process is one which involves two photons of low energy combining to form one photon of a higher energy. The upconversion process we shall concern ourselves with is second harmonic generation, which provides an intuitive way of examining many processes relevant to nonlinear optics. Phase matching in particular is best described in regards to second harmonic generation and the discussions will apply equally to downconversion processes.

3.3.1 SHG

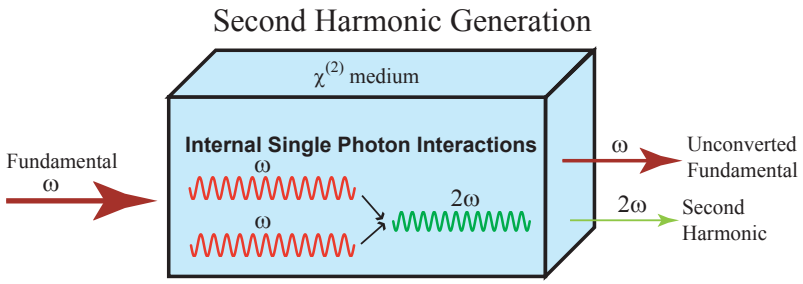

Figure 3.1: Second Harmonic Generation. SHG involves two photons of frequency ω, which can be from the same beam, combining to create one photon of frequency 2ω.

Second harmonic generation is the process of two photons of equal energy combining to result in one higher energy photon. The process is depicted in figure 3.1. At the input we have one beam of frequency ω entering the face of the crystal. Inside the nonlinear medium the process that we want to encourage is two photons from the input fundamental combining to produce one photon at the second harmonic. In second harmonic generation only a proportion of the fundamental is converted to the second harmonic and this is why there is still a large amount of fundamental power exiting the medium in this figure. Single-pass experiments, in which the light incident on the medium only passes through once, are able to achieve efficiencies of approximately forty percent [13].

3.4 Downconversion processes

Downconversion processes are the complementary processes to upconversion. In a downconversion process, one photon is split into two photons of lower energy. We now explore in detail the degenerate and non-degenerate optical parametric amplifiers and the optical parametric oscillator.

3.4.1 DOPA

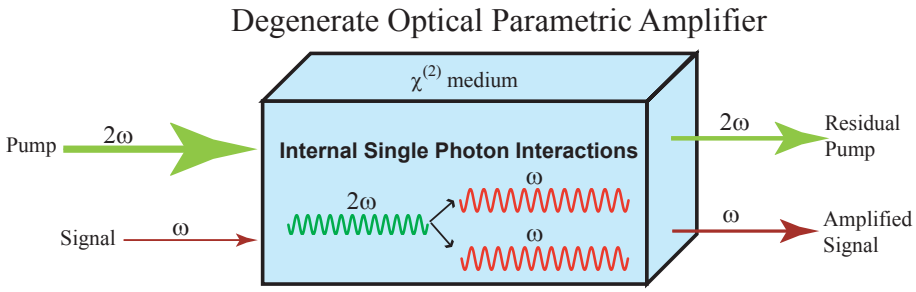

Figure 3.2: The degenerate optical parametric amplifier. The signal and the pump beam are incident on the $\chi^{(2)}$ medium. Inside the medium we note that a single photon of frequency 2ω is converted into two photons of frequency ω.

First, we will look at the degenerate optical parametric amplifier as shown in figure 3.2. We note that there is both a pump and a signal beam incident on the medium. The thickness of the beams is a rough indication of their intensities, most experiments require that the intensity of the pump be much larger than the intensity of the seed in order to prevent the amplification process from reversing. Inside the medium, a three photon interaction occurs. A single photon of frequency ω_{pump} is converted into two photons of frequency ω_{signal}. This is known as a downconversion process because a photon of higher energy is converted to two photons, each one of less energy than the original photon. The process of the pump photon splitting into two other photons causes quantum correlations between the sidebands around the frequency ω to arise, and is the cause of squeezing. Conservation of energy is ensured by having the frequency of the pump photon equal to the combined frequency of the two photons created in the process. For the degenerate case we can write

$$\omega_{pump} = \omega_{signal} + \omega_{signal} \tag{3.3}$$

Now we look at the output of the medium. There is still a residual pump beam as only a portion of the pump photons will be converted into signal frequency photons. Recall however, that the intensity of the pump was much larger than the intensity of the input signal beam, so a small proportion of converted pump photons may have a large impact on the intensity of the signal beam. The pump beam will also be depleted by a minute amount, though most cavity calculations assume that the power depletion in the pump mode is so minute that for all intents and purposes we can treat the intensity of the pump field as a constant. The input beams are generally assumed to be coherent states and it is important to note that fluctuations across all frequencies will be present for all of these

processes.

3.4.2 NDOPA

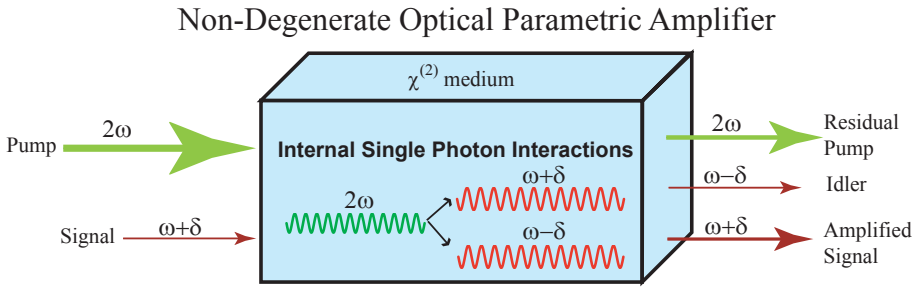

Figure 3.3: The non-degenerate optical parametric amplifier. Note that, as opposed to the DOPA, the pump beam now primarily splits into two non-degenerate photons of frequency $\omega+\delta$ and $\omega-\delta$ where $|\delta| < \omega$.

Fig. 3.3 shows the important fields for the non-degenerate optical parametric amplifier, the process is also known as difference frequency generation. The only alteration between this setup and the setup in the DOPA is that the signal beam is no longer at exactly half the frequency of the pump beam. The effect this has is that when amplification occurs, through the splitting of one of the pump photons, one will be at the frequency of the signal, and one will be at the difference frequency of the pump and the signal. This difference frequency is known as the idler frequency. We can write

$$\omega_{pump} = \overbrace{(\omega+\delta)}^{signal} + \overbrace{(\omega-\delta)}^{idler} \tag{3.4}$$

or equivalently, in order to make the difference frequency generation process more apparent

$$\omega_{pump} - \overbrace{(\omega+\delta)}^{signal} = \overbrace{(\omega-\delta)}^{idler} \tag{3.5}$$

3.4.3 OPO

Moving onto the optical parametric oscillator as shown in fig. 3.4, we note that the major difference between the OPO and the OPA is that the input coherent beam is now the vacuum state. Also, the OPO by definition contains the nonlinear medium in a cavity, whereas the OPA need not. The OPO generates vacuum squeezing, which is conceptually more difficult than the squeezing in the OPA, but which can be reduced to case of the OPA with the right framework. Recall that in the NDOPA the primary process which occurs in order to achieve amplification, is the downconversion of a pump photon into a signal and an idler photon. In the degenerate case the idler frequency was at the signal frequency. This, however, is not the only process which occurs. The fluctuations in the coherent field, depicted in figure 2.7 also play a role in the process. Indeed it is the interaction with these fluctuations which allows us to produce squeezing. We have previously seen that the vacuum state has a variance of one in both quadratures.

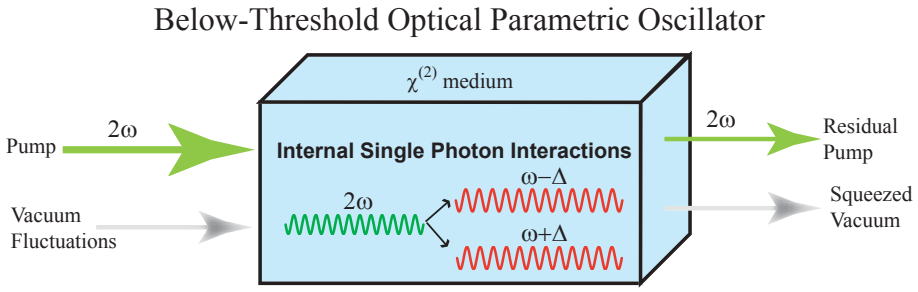

Figure 3.4: The optical parametric oscillator. Only a pump beam and vacuum fluctuations are incident on the $\chi^{(2)}$ medium. Inside the medium we note that a single photon of frequency 2ω is converted into two photons of frequency $\omega + \Delta$ and $\omega - \Delta$ for all $\Delta < \omega$.

$$\Delta^2 X^+_{vac} \Delta^2 X^-_{vac} = 1 \tag{3.6}$$

A conceptually simple way of visualizing the process is to think of the vacuum state as just an alternative input to the NDOPA. The only difference is that the vacuum state contains fluctuations at all frequencies without a strong field at any particular frequency, so there is an equal chance of converting a pump photon into any two photons with energies given by

$$2\omega_{pump} = (\omega + \Delta_{vac}) + (\omega - \Delta_{vac}) \tag{3.7}$$

where Δ is all frequencies $< \omega$.

The effect this has is to correlate the sidebands around half the pump frequency, this is shown in figure 3.5. At higher frequencies, it is the linewidth of the cavity which will limit the range of squeezing which can be observed. At low frequencies it will be effects such as scattered radiation which will limit the detection of squeezing [14]. Recalling that the squeezed vacuum has a photon number equal to $sinh^2 r$, equation 2.43, it becomes apparent that this method of visualizing the squeezing process explains the nonzero average photon number for a squeezed vacuum state.

3.5 Nonlinear interactions in the sideband picture

The sideband picture for the squeezing process due to an OPA interaction is shown in figure 3.5. First we note that fluctuations are still present for all frequencies as depicted by the black arrows. A quantum picture of the modulations in figure 2.5 would also include these fluctuations across all ω. In all downconversion squeezing processes we will have a strong field at a frequency of ω_{pump}. We will first use this figure to explain the DOPA process. In the DOPA there will also be a field present at $\omega_{signal} = \frac{1}{2}\omega_{pump}$, the primary process occurring will be the removal of photons from the pump and the creation photons at the signal frequency. However, fluctuations in the coherent field will also cause some pump photons to split into photon pairs at $\omega_{signal} + \Delta$ and $\omega_{signal} - \Delta$ for all $0 \leq \Delta \leq \omega_{signal}$. These sideband pairs are represented in figure 3.5 as sidebands of the same colour and similar arrowheads, and are centred about ω_{signal}. It is these correlated sidebands which are the cause of squeezing. If the correlated sidebands tend to align in the imaginary axis then they must also tend to misalign in the real axis and hence we have reduced the

fluctuations in the amplitude quadrature. In this way we can think of amplitude squeezing as a broad spectrum phase modulation of the previously uncorrelated sidebands.

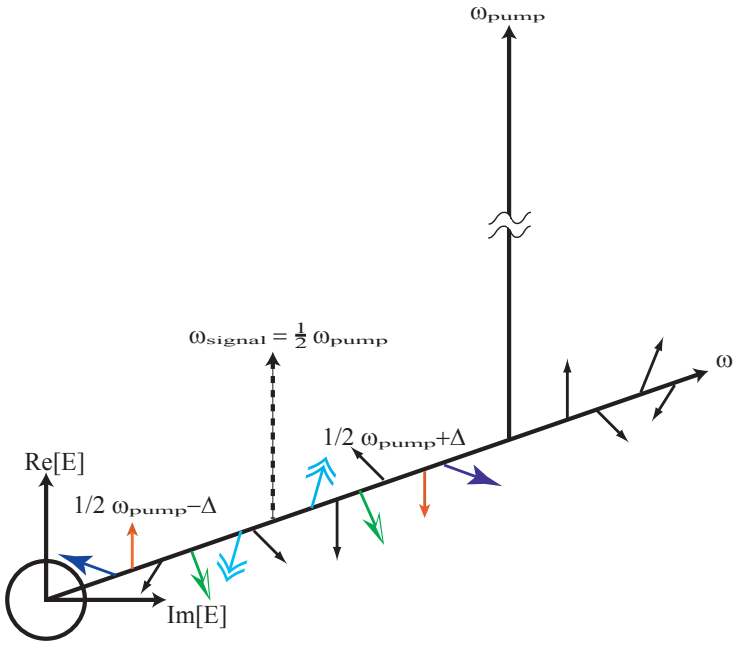

Figure 3.5: Squeezing in the sideband picture. Depicted is squeezing due to a DOPA setup. A strong field at ω_{pump} is split into photon pairs which amplify the field at $\omega_{signal} = \frac{1}{2}\omega_{pump}$. At the same time some photons in the pump are split into photon pairs at $\omega_{signal} + \Delta$ and $\omega_{signal} - \Delta$ for all $0 \leq \Delta \leq \omega_{signal}$. These correlated sidebands have the effect of reducing the fluctuations at some angle and are the cause of the squeezing.

Figure 3.5 can easily be generalised to describe squeezing in the OPO and NDOPA. In the case of the OPO all we need do is remove the dashed field at ω_{signal} so that the only process occurring is the downconversion of the pump due to the vacuum fluctuations. In the same way as the DOPA, we will produce correlated sidebands centred around $\frac{1}{2}\omega_{pump}$. In the case of the NDOPA we simply add two bright fields at the frequencies $\frac{1}{2}\omega_{pump} + \delta$ and $\frac{1}{2}\omega_{pump} - \delta$, for any delta $0 < \delta < \omega_{signal}$, to indicate that the downconversion process is producing amplification of the fields at these frequencies. The argument behind the squeezing is still exactly the same and the squeezing is still centred around $\frac{1}{2}\omega_{pump}$.

3.6 Phase matching

Thus far in our coverage of the nonlinear processes, we have only concerned ourselves with conservation of energy. This was done by ensuring the energy of each pump photon was equal to the energy of the two photons it converted into. The processes must also conserve momentum, however, and this is achieved through the technique of phase matching.

Dispersion in the nonlinear medium is the major cause of poor phase matching. The fundamental and second harmonic beams will see different refractive indices as they travel through the medium and hence one of the waves will be moving faster than the other. This will effectively reduce the interaction length of the nonlinear process. In turn, this will

have the effect of drastically reducing the efficiency of any nonlinear process. One method of overcoming this problem is to use a birefringent material. In a birefringent material we can define a principal plane as the plane containing the optic axis and the propagating light beam. If light directed down the optic axis is polarised in this plane then it is known as an extraordinary beam and if it is polarised normal to this plane then it is known as an ordinary beam. The refractive indices for the two beams is different and the refractive index of the extraordinary beam is dependant upon the angle between the optic axis and the direction that the light is propagating. The refractive index for the ordinary beam, however, is not sensitive to beam direction and by tuning the angle between the optic axis and the beam propagation direction, in many materials a phase matching condition known as angle-tuned phase matching can be found.

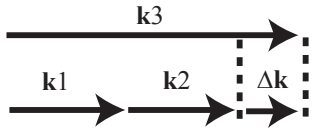

Figure 3.6: Phase vectors. The phase mismatch vector Δk accounts for the momentum mismatch between the signal and idler photons and the pump photon

Figure 3.6 shows the phase matching scheme for collinearly propagating beams. To be perfectly phase matched we require that $\Delta\vec{k} = 0$. The effects of poor phase matching are most easily explored in the case of SHG, but are also going to adversely affect the outcome of any of the other nonlinear interactions. In all of the nonlinear processes there is a property known as the coherence length, L_c, but for simplicity we shall explain it first in terms of SHG. In SHG, the coherence length is a measure of how far into the crystal the light beam with the fundamental frequency will travel, whilst generating the second harmonic, before the process will reverse and the second harmonic which has been produced will couple back into the fundamental. The coherence length is given by

$$L_c = \frac{\pi}{\Delta k} \tag{3.8}$$

where Δk is the magnitude of the phase mismatch of the system. The greater the value of Δk, the less the amount of fundamental power converted to the second harmonic before the process begins to reverse. Figure 3.7 illustrates this point.

In figure 3.7, the intensity of the second harmonic as a function of distance into a nonlinear material is plotted. We see that if the phase mismatch, Δk, is small, the maximum intensity of the second harmonic is much greater. Also, the coherence length for small mismatches is much larger. At twice the coherence length, the process of second harmonic generation has been completely reversed and the net gain in the second harmonic is zero. For this reason, when manufacturing a crystal to be used with conventional phase matching techniques, if an estimate of the expected phase mismatch can be found then the length of the crystal should not exceed the coherence length.

Figure 3.7 showed that the maximum intensity of the second harmonic achievable in SHG is strongly dependant upon the value of Δk. With this in mind, the efficiency of the second harmonic generation can be plotted. We define the efficiency as the ratio of the intensity of the second harmonic as a function of L, the distance into the crystal, to the

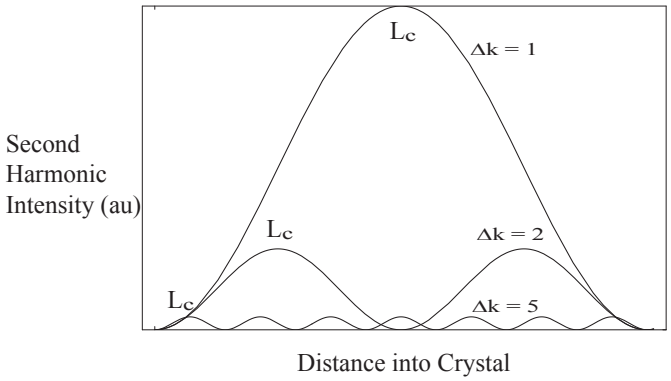

Figure 3.7: Effect of phase mismatch on the maximum intensity achievable in SHG. 3 lines are drawn for 3 different values of Δk. Note that as Δk increases the maximum second harmonic intensity is reduced and the coherence length L_c shortens. The coherence length is the length into the crystal where the upconversion process reverses and downconversion dominates.

initial intensity of the fundamental. It can be shown [11] that

$$\frac{I_{SH}(L)}{I_F(0)} \propto sinc^2\left(\frac{\Delta k L}{2\pi}\right) \tag{3.9}$$

where the sinc function is defined as, $sinc(x) = \frac{sin(\pi x)}{\pi x}$.

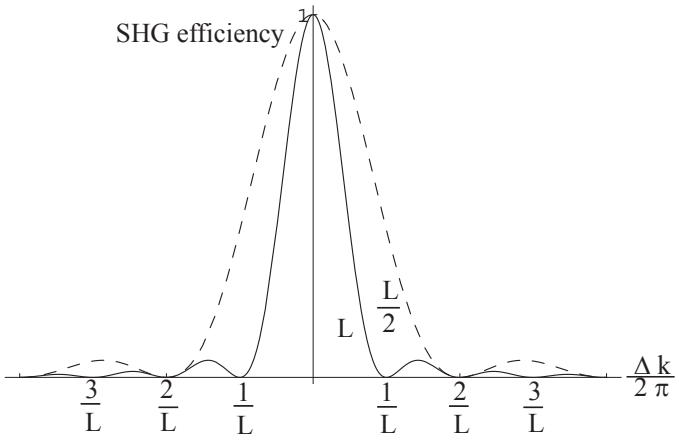

Figure 3.8: Normalized SHG efficiency. For the two crystals, one of length L and the other of length $\frac{L}{2}$, it is apparent that phase matching becomes more sensitive to phase mismatches in the longer crystal, indicated by the narrowness of the maximum efficiency peak.

Figure 3.8 shows the second harmonic efficiency as a function of $\frac{\Delta k}{2\pi}$. The solid line is the efficiency for a crystal of length L, and the dotted line is the efficiency for a crystal of length $\frac{L}{2}$. First note that for large phase mismatches, the efficiency drops drastically. Also of importance is that the efficiency is more sensitive to phase mismatches as L increases, this has a large impact on designing any of the aforementioned nonlinear interaction

experiments. We see that the shorter crystal has a much broader profile, which indicates that there is less sensitivity to phase mismatch. Whilst a longer crystal may offer a possibly longer interaction length, the longer the crystal, the harder phase matching becomes. When choosing crystal length, a trade-off between the two optimisations must be found. This effect is very important in quasi-phase matching.

3.6.1 Quasi-Phase Matching

One of the major problems with standard phase matching techniques, such as angle tuning, is that the direction through the crystal which satisfies phase matching conditions is not likely to be the direction with the strongest nonlinearity coefficient. In many of the materials there is one direction through the crystal in particular which exhibits a very strong nonlinear coefficient. Standard phase matching techniques generally do not allow for the use of this direction through the crystal and as such the crystals cannot be used to their full potentials. First conjectured in 1962 [4], a solution to this problem was realised, coined quasi-phase matching. Rather than try to find a direction through the crystal where phase matching could be achieved, the technique of quasi-phase matching compensates for not operating under phase matched conditions. Figure 3.7 introduced the concept of the coherence length, L_c. This length was defined as the length into the crystal where the SHG process began to reverse and the second harmonic which had been generated began to couple back into the fundamental. In general, for any nonlinear process the coherence length is defined as the point in the crystal where the nonlinear process which occurred up to that point in the crystal is reversed. Eventually, at twice the coherence length, any powers generated by the nonlinear process have been coupled back into the initial field. In quasi-phase matching, rather than aim for a non-zero phase mismatch, the idea is to compensate for a non-zero phase mismatch by effectively reversing the sign of the second order nonlinearity at periodic intervals down the length of the crystal. By reversing the sign of the second order nonlinearity at every coherence length, the back-conversion which was otherwise going to occur, is reversed, and instead the desired nonlinear process continues to occur. The techniques for reversing the sign of the nonlinearity are discussed in chapter 4. Figure 3.9 shows how ideal PM and first order QPM affect the generated second harmonic.

Firstly, we note that the phase matching in figure 3.9 is first order phase matching. This means that the domains have been inverted at every coherence length. This is the most efficient form of quasi-phase matching and because of this is obviously the preferred method. Sometimes, however, it may be impractical to pole the material at every coherence length, if for example the phase mismatch is large. A large phase mismatch, as discussed previously, will reduce the coherence length. Using current techniques there is a limit to the minimum width of the domains in the poled materials, and is in fact dependant upon the material being poled. In cases where first order periodic poling is not feasible, it may be useful to do third order electric field periodic poling, which consists of creating inversion domains which have a width of three coherence lengths.

It can be shown that the intensity of the second harmonic in the ideal phase matched case will grow as the square of the length of the crystal [15].

$$I_{SH} \propto L^2 \tag{3.10}$$

It can also be shown that in the ideal quasi-phase matched case, the intensity grows as

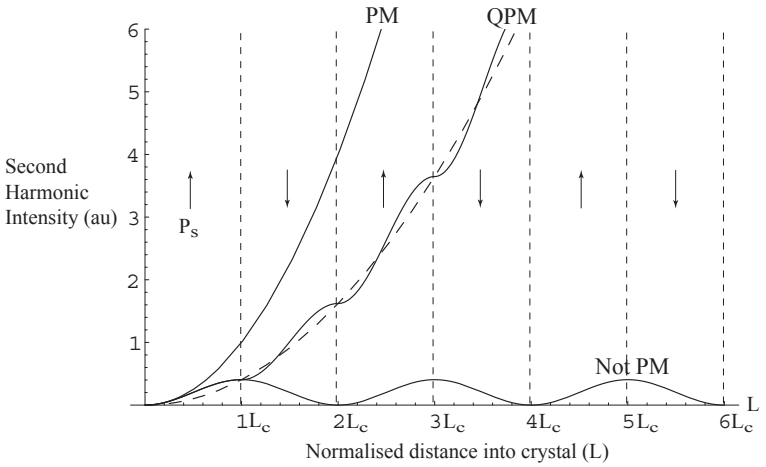

Figure 3.9: Efficiencies of PM and QPM in SHG. Ideal standard PM grows as L^2 whereas ideal first order QPM will grow as $\left(\frac{2L}{\pi}\right)^2$.

the length squared, multiplied by a factor

$$I_{SH} \propto \left(\frac{2L}{m\pi}\right)^2 \tag{3.11}$$

where m is the order of the phase matching. For example, $m = 1$ in first order phase matching.

This plot can be misleading, in that it appears standard phase matching is ideal, but it doesn't take many other factors into account. Not the least of these factors is that QPM allows for directions in the crystals with very high strength second order nonlinearities to be utilized which would otherwise be unusable with standard PM techniques. In this plot it is assumed that the initial strength of the second order nonlinearity for each case is equal. At the same time the QPM case assumes perfect domain widths created by the poling process and whilst current techniques are getting better, they are certainly not perfect, and hence the second harmonic growth in figure 3.9 indicates only the limit for perfect phase matching, it doesn't indicate how imperfect domains affect second harmonic generation. The effects brought about by imperfect phase matching are explored further in [15]. That said, it is still normally the case that QPM will allow access to stronger effective second order nonlinearities than standard PM, and as such periodically poled materials are becoming more common in nonlinear optical experiments.

Nonlinear materials

One of the aims of this thesis was to compare different nonlinear materials in the hope that distinctions between the materials could be found. This chapter provides a background into some of the history of the materials to be used and some of their properties. Quasi-phase matching was introduced in chapter 3 without any discussion on the methods used for flipping the sign of the second order nonlinearity. In this chapter we also investigate the methods used to change the sign of the second order nonlinearity.

4.1 The poling process

Quasi-phase matching requires that the sign of the second order nonlinearity in a nonlinear material be changed at multiples of the coherence length through the crystal. Perhaps the most obvious method would be to stick wafers whose thickness is equal to the coherence length together, having alternating wafers rotated by 180°. There are methods which are based on this approach [16] but there is also another method which tends to produce more consistent domain periods. This method is known as electric field periodic poling and is realisable in many ferroelectric crystals. The idea is to create periodic domains within the crystal in which the spontaneous polarisation. P_S is reversed. This is shown in figure 4.1. The reversal of the spontaneous polarisation direction is achieved through the application

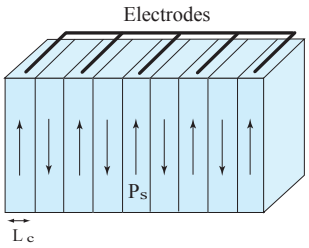

Figure 4.1: Domain Inversion

of very strong electric fields through the use of thin electrodes placed at intervals on the surface of the crystal. If a strong electric field is applied by the electrodes, then we can create the domain structure shown in figure 4.1. The arrows indicate the direction of the spontaneous polarization P_s domains. Figure 4.1 shows the case of a first order phase matched material, as the domain widths are equal to the coherence length, L_c.

There are many factors which influence how effective an electric field periodic poling run is. The first major factor is the magnitude of the phase mismatch. The greater the

phase mismatch, the smaller the coherence length. This means that the width of the poling domains is necessarily going to have to be shorter. Electric fields on the order of tens of kilovolts per metre are applied to the crystal and as the domain periods become smaller, the spacing between electrodes must also become smaller and the chance of arcing becomes greater. Smaller domain inversion periods are also harder to achieve because of the nature of domain growth, this is explored by Miller [6]. Yet another limiting factor in electric field periodic poling is the height of the crystal being poled. In order for straight, even inversion domains to grow, it is necessary that the thickness of the crystal is limited. This factor means that, depending upon the crystal begin poled, its thickness may be limited to perhaps fractions of a millimetre in order to achieve straight domain walls.

4.2 Periodically poled 1.7 percent MgO doped stoichiometric lithium niobate

Also known as MgO:PPSLN. This is the newest material out of the three to be tested and has been modified in many ways in order to tailor its properties for efficient second order nonlinear interactions. The crystal is stoichiometric which means that the ratio of lithium to niobium atoms in the growth is close to fifty percent,

$$\frac{[Li]}{[Li]+[Nb]} \approx 0.50 \tag{4.1}$$

where [Li] indicates the concentration of lithium in the growth. A congruent crystal will have equation 4.1 tend more towards a value of 0.48. Having a stoichiometric crystal implies that there are less defects present in the material, and as such will generally have a higher optical damage threshold than a congruent growth. The damage threshold is a measure of the optical power needed in a material to cause photorefractive damage. Doping the crystal with magnesium oxide raises the damage threshold by reducing substitutional defects in the crystal structure [17]. With a stoichiometric growth and low levels of magnesium oxide doping, it has been shown that the optical damage threshold for lithium niobate is greater than $8000 kW/cm^2$ [17]. The highest nonlinear coefficient in 1 percent magnesium oxide doped congruent lithium niobate is in the d_{33} direction and is found to be $24.9 pM/V$ for a 1064nm fundamental in SHG [18]. As the 1.7% doped stoichiometric material is new, no data could be found containing the exact value of its nonlinear coefficient. It will be assumed that $24.9 pM/V$ is a fair approximation to its true value. It has been shown with stoichiometric growths that some of the nonlinear coefficients can increase as the crystal approaches perfect stoichiometry [19] and as such the nonlinear coefficient may be larger than this value. Oxide corporation [20] claim that their SLN crystals have a nonlinear coefficient greater than $34.1 pm/V$ but it was decided to use the value of $24.9 pm/V$ in the models because this was the highest value that could be found in a paper describing the measurement of this value. The crystal to be used in this experiment is 9.5mm long by 7mm wide by 0.5mm thick. It was supplied by OXIDE Corporation Japan and has varying poling periods along the crystal length with different phase matching temperatures. The highest levels of squeezing to date, have been achieved with an unpoled monolithic 7 percent $MgO : LiNbO_3$ [21].

4.3 Wedged periodically poled stoichiometric lithium tantalate

Abbreviated to PPSLT. This material has also been periodically poled so that the direction through the crystal with the highest nonlinear coefficient may be used. This is in the d_{33} direction and for congruent lithium tantalate is $13.8pm/V$ [18], but it is believed that the nonlinear coefficient for stoichiometric lithium tantalate may be higher than for congruent lithium tantalate [22]. Oxide corporation [20] state that their SLT has a second order nonlinear coefficient of $26.2pm/V$, although we agin opt to use a value of $13.8pm/V$ in the models because no papers could be found experimentally supporting this claim. Also of importance is that one edge of this crystal is wedged, which should theoretically allow for cavity dispersion compensation. No information could be found indicating that wedged materials have previously been used in travelling wave OPO experiments. This crystal was 10mm in length by 5mm in width by 1mm in height, and was supplied by Raicol Crystals. The stoichiometric growth also aids in the poling of thicker crystals, such as this one. This is because the stoichiometric growth reduces the strength of the electric field required to invert the domains within the crystal [22].

4.3.1 Wedged crystals

The wedge is made by polishing one end of the crystal at an angle of $\theta = 1.15°$ to the poling domains, so that as the crystal is translated, the optical path length through the crystal varies. Whilst phase matching compensates for dispersion inside the nonlinear medium, the two waves will pick up differing phase shifts in one round trip of the cavity due to mirror reflections and to a lesser extent dispersion in air, the wedge is designed to compensate for this effect. The translation of this crystal allows for a position through the crystal to be found, where the dispersion due to the cavity is overcome. This all relies upon the fact that dispersion is inherent in any quasi-phase matched material. The coherence length, L_c, was defined as a measure of how far into the crystal a nonlinear process such as SHG would occur for two given wavelengths, before the process would reverse. The process reverses because the phase of the two beams has changed by a factor of π over this length due to the difference in the refractive indices for the two beams. By changing the length that the two beams travel in the last domain, their phase relationship upon exiting the crystal is also varied and this can be used to compensate for the dispersion due to the cavity.

4.4 Periodically poled potassium titanyl phosphate

PPKTP is the final crystal to be tested in the experiment. The highest nonlinear coefficient is again the d_{33} component and this time is equal to $14.6pm/V$ [18]. This crystal has been used fairly recently to obtain squeezing levels of 7dB by Suzuki *et al* [23]. This material was not wedged, which gave the PPSLT a slight advantage over the PPKTP, in that conditions closer to the optimum could theoretically be achieved with the PPSLT. This crystal was also grown by Raicol Crystals and it was 10mm in length, by 2mm wide by 1mm in height.

The optical cavity

In this chapter we look at the equations of motion for an optical cavity, both with and without a nonlinear medium at its focus, derived using the quantum Langevin method. Here we will only investigate the important features and the reader is referred to previous work by Buchler [9] and Gardiner [24] for a more thorough background. A brief overview of the quantum Langevin method is first given and the arising cavity decay rates are discussed. From there we show how the optical cavity can be used as a low pass filter and then explore how squeezing in the DOPA and OPO can be improved by tailoring the reflectivities of the input and output couplers for the signal/idler and pump beams.

5.1 Method for deriving cavity equations

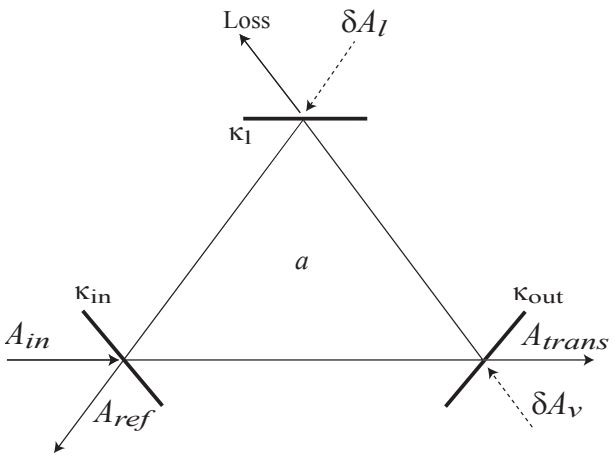

Figure 5.1: Fields interacting with three mirror ring cavity. The only bright input is the coherent fundamental mode, A_{in}.

The quantum Langevin method for deriving the cavity equations assumes that the quantum system in question is in contact with a heat bath which acts irreversibly on that system. It is the terms which represent the irreversible processes that conserve the quantum mechanical requirements of the system. The important result from the quantum Langevin treatment is that any external field entering our cavity will be multiplied by a factor of

$$\sqrt{2\kappa} \tag{5.1}$$

where κ is the decay or damping rate of a given mode and whose definition relies upon the mean field approximation which is explored further in section 5.1.1. Figure 5.1 shows the important fields in the cavity system with one bright beam entering the system. A three mirror ring cavity is depicted because it simplifies the visualisation of all of the interacting fields. The equations hold equally as well for linear cavities and for bow-tie cavities, such as the one used in this thesis. The A operators represent the fundamental frequency traveling wave fields interacting with the cavity. The subscripts in, ref and $trans$ indicate the input, reflected and transmitted fields respectively. The δA_l term indicates the vacuum state entering the cavity due to losses in the system and the δA_v term indicates the vacuum term entering the cavity at the output coupler. Note that these two vacuum terms will be uncorrelated. The a inside the cavity represents the intra-cavity fundamental mode.

Through the quantum Langevin treatment, it is also possible to derive [24]

$$\tilde{A}_{ref} = \sqrt{2\kappa_{in}}\tilde{a} - \tilde{A}_{in} \tag{5.2}$$

$$\tilde{A}_{trans} = \sqrt{2\kappa_{out}}\tilde{a} - \delta\tilde{A}_v \tag{5.3}$$

which can be used to relate the intra-cavity field to the transmitted or reflected field.

5.1.1 Cavity damping rates

In order for the cavity equations to be of any use in an experiment, we need to be able to relate the cavity damping rates to measurable parameters. The cavity decay rates, κ, are defined in terms of the cavity round trip time and the reflectivity of the mirror or mirrors in question. Losses may be modelled as a beamsplitter, the transmission of which will depend upon the magnitude of the loss. The round trip time is defined as

$$\tau = \frac{nL}{c} \tag{5.4}$$

where n is the refractive index that the light experiences within the cavity, L is the length of one round-trip of the cavity and c is the speed of light in vacuum. The decay rate in its entirety is an infinite Taylor expansion, from which generally only the first two terms are retained. Provided that the reflectivities do not approach 0, this reduction is valid. After reducing the Taylor expansion, the decay rate can then be defined in a number of ways. For an in-depth discussion of the properties of each definition, the reader is directed to previous work undertaken by White [12]. The limitation to these definitions and in fact, the whole concept of the cavity decay rate, is that it relies on the mean field approximation (MFA). This approximation assumes that losses through one round trip of the cavity are not large and that losses are not localized. These assumptions are valid with highly reflective mirrors but break down as the mirror reflectivities approach zero. The definition of the cavity decay rate used in this thesis is

$$\kappa = \frac{1}{\tau}\left(1 - \sqrt{R}\right) \tag{5.5}$$

where R is the reflectivity of the mirror. This definition is chosen because it provides a reasonable definition for moderate reflectivities and is very accurate at high reflectivities, resulting in a broad region of suitability.

5.2 The bow-tie cavity

A bow-tie cavity was the best cavity design for this experiment mainly due to the ease it afforded in switching nonlinear crystals but also because of the seeding options it allowed. Figure 5.2 shows the bow-tie cavity operating as an OPO with the important fields illustrated The vacuum state, which acts as the seed for the OPO system, is not illustrated in

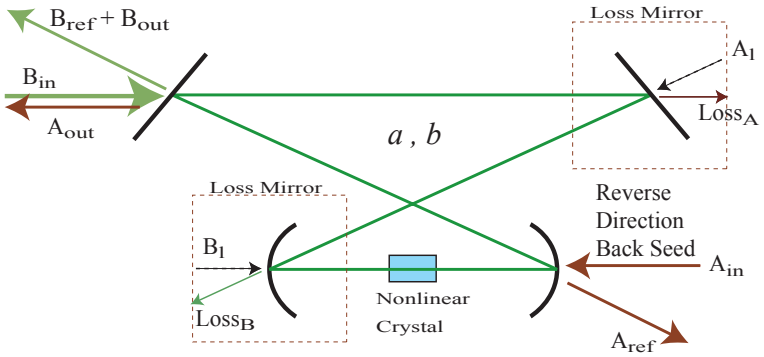

Figure 5.2: Bow-tie cavity fields in an OPO setup.

the figure so as not to overcrowd the diagram. The two mirrors which are not used as input or output couplers can be effectively treated as one mirror in all equations, and as such have been boxed and labelled as the loss mirrors. Making this assumption, the bow-tie cavity is reduced to exactly the ring cavity shown in figure 5.1, and the mathematics is left unchanged. The experimental setup utilised a reverse direction back seed in order to lock the cavity length to the fundamental frequency. The fact that the seed propagates in the reverse direction in comparison with the pump, means that it will take no part in the nonlinear interaction. In this way we can construct an OPO setup while stil using the fundamental reverse seed to lock the cavity.

5.3 Cavity equations

Here we state the full quantum cavity equations as found using the quantum Langevin method [24, 9] for an empty cavity. In this representation of the equations, we have moved into a rotating frame, with a frequency equal to that of the carrier.

$$\dot{a} = i\Delta_a a - \kappa_a a + \sqrt{2\kappa^a_{in}} A_{in} + \sqrt{2\kappa^a_{out}}\delta A_{vac} + \sqrt{2\kappa^a_{loss}}\delta A_{loss}$$

Note that the external fields interacting with the cavity have been multiplied by their corresponding factors from equation 5.1. In the equation, $\dot{a}$ is the time derivative of the operator a, whilst Δ_a represents the frequency mismatch of the fields a from the value set by the length of the cavity, we can write

$$\Delta_a = \omega_{seed} - \omega_{ideal} \tag{5.6}$$

$$\tag{5.7}$$

where ω_{ideal} is the frequency for the seed at which there will be no mismatch with the resonance frequency set by the length of the cavity.

5.3.1 Noise properties of optical cavities

In order to examine the noise properties of the cavity, the aim is to find an expression for the amplitude quadrature spectrum of the reflected and transmitted modes, V_{Aref} and V_{Atrans} respectively. As we are only interested in the noise of the field, the first step is to linearise the operators so that only the first order fluctuating terms are retained. This results in

$$\delta\dot{a} = i\Delta_a\delta a - \kappa_a\delta a + \sqrt{2\kappa^a_{in}}\delta A_{in} + \sqrt{2\kappa^a_{out}}\delta A_{vac} + \sqrt{2\kappa^a_{loss}}\delta A_{loss} \tag{5.8}$$

The fluctuating part of the amplitude quadrature operator is then found, using $\delta X^+_a = \delta a + \delta a^\dagger$, a generalization of equation 2.17,

$$\delta\dot{X}^+_a = i\Delta_a\delta X^+_a - \kappa_a\delta X^+_a + \sqrt{2\kappa^a_{in}}\delta X_{Ain} + \sqrt{2\kappa^a_{out}}\delta X_{Avac} + \sqrt{2\kappa^a_{loss}}\delta X_{Aloss} \tag{5.9}$$

Using the linearity property of the Fourier transform and equation 2.17 we now define the frequency domain amplitude quadrature operator as

$$\tilde{X}^+(\omega) = \mathcal{F}[X^+(t)] = \mathcal{F}[A(t)] + \mathcal{F}[A^\dagger(\omega)] \tag{5.10}$$

where the tildes have been used to indicate that the operator is now in the frequency domain. We also make use of two important properties of the Fourier transform,

$$\mathcal{F}[\dot{a}(t)] = i\omega\tilde{a}(\omega) \tag{5.11}$$

$$\mathcal{F}[c^*(t)] = \tilde{c}^*(-\omega) \tag{5.12}$$

where c is some complex function. Using Equation 5.12 we can now write

$$\mathcal{F}[A^\dagger(t)] = \tilde{A}^\dagger(-\omega) \tag{5.13}$$

Taking the Fourier transform of equation 5.9 results in

$$(i\omega - i\Delta_a + \kappa_a)\delta\tilde{X}^+_a = \sqrt{2\kappa^a_{in}}\delta\tilde{X}_{Ain} + \sqrt{2\kappa^a_{out}}\delta\tilde{X}^+_{Avac} + \sqrt{2\kappa^a_{loss}}\delta\tilde{X}^+_{Aloss} \tag{5.14}$$

and using the input/output relations from equations 5.3 and 5.2 gives

$$\delta\tilde{X}^+_{ref} = \frac{\left(2\kappa^a_{in} - \kappa_a - i\omega + i\Delta_A\right)\delta\tilde{X}^+_{Ain} 2\sqrt{\kappa^a_{in}\kappa^a_{out}}\delta\tilde{X}^+_{Avac} + 2\sqrt{\kappa^a_{in}\kappa^a_{loss}}\delta\tilde{X}^+_{Aloss}}{i\omega + \kappa_a - i\Delta_a} \tag{5.15}$$

$$\delta\tilde{X}^+_{trans} = \frac{2\sqrt{\kappa^a_{out}\kappa^a_{in}}\delta\tilde{X}^+_{Ain} + \left(2\kappa^a_{out} - \kappa_a - i\omega + i\Delta_A\right)\delta\tilde{X}^+_{Avac} + 2\sqrt{\kappa^a_{out}\kappa^a_{loss}}\delta\tilde{X}^+_{Aloss}}{i\omega + \kappa_a - i\Delta_a} \tag{5.16}$$

The final step is to define the output spectrum

$$V^+_A = \langle|\delta\tilde{X}^+|^2\rangle \tag{5.17}$$

and recalling that $\delta\tilde{X}^+_{Aloss}$ and $\delta\tilde{X}^+_{Avac}$ are uncorrelated vacuum terms, we finally reach

$$V^+_{Aref} = 1 + \frac{\left((2\kappa^a_{in} - \kappa_a)^2 + (\Delta_a - \omega)^2\right)\left(V^+_{Ain} - 1\right)}{\kappa_a^2 + (\Delta_a - \omega)^2} \tag{5.18}$$

$$V^+_{Atrans} = 1 + \frac{4\kappa^a_{out}\kappa^a_{in}\left(V^+_{Ain} - 1\right)}{\kappa_a^2 + \left(\Delta_a - \omega\right)^2} \tag{5.19}$$

We can now plot the noise response for the reflected and transmitted beams as a function of the frequency of the laser.

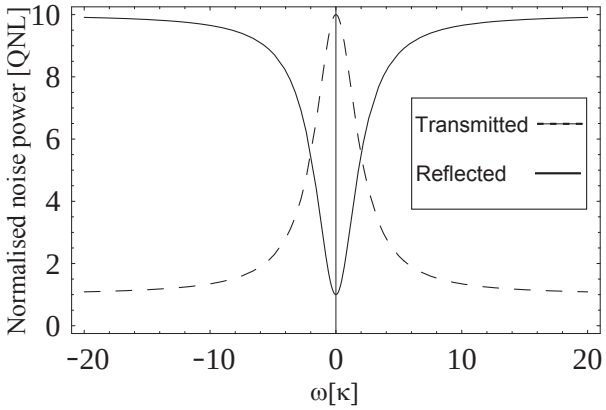

Figure 5.3: The noise response of a cavity. The chosen values are $\kappa^a_{in} = \kappa^a_{out} = 1$, $\kappa^a_{loss} = 0$, $\Delta_a = 0$ and $V_{Ain} = 10$.

From figure 5.3 we can see that a cavity with low decay rates will act as a low pass filter for the laser when the cavity and the laser are co-resonant. This setup is commonly known as a mode cleaner cavity because it will strip the high frequency noise off the laser. The smaller the total cavity decay rate, κ, the stronger this effect is and the narrower the linewidth of the cavity, resulting in a lower cut-off frequency. Another effect of the mode cleaner which is not shown in a basic noise treatment, is its ability to clean the spatial mode of a propagating beam. When the cavity is exactly on resonance, generally only one spatial mode of light will be resonant, we can use this property to exclusively transmit the $(0, 0)$ Hermite-Gaussian mode [11] of light, which is the Gaussian beam. The Gaussian beam is also known as the (0,0) transverse electro-magnetic mode, or TEM_{00} mode.

It is desirable to have the losses in such a mode cleaner as low as possible, so that optical power is not needlessly wasted. A common property of a cavity, which is a measure of the losses, is known as the finesse, $\mathfrak{F}$. For a cavity with a nonlinear medium at the focus, the finesse can be defined as [11]

$$\mathfrak{F} = \frac{\pi r^{\frac{1}{2}}}{1 - r} \tag{5.20}$$

where r is the overall intensity attenuation factor and assuming that propagation through air is lossless, is defined as,

$$r^2 = \left(\prod_k \mathfrak{R}_k\right) \exp^{-2\alpha_s d} \tag{5.21}$$

where the $\mathfrak{R}_k$ are the mirror reflectivities encountered in one round trip of the cavity, α_s is the absorption coefficient of the crystal in the cavity and d is the distance the light travels through the crystal. The finesse can also be measured as the ratio of the free spectral range and the full width at half maximum of the cavity

$$\mathfrak{F} = \frac{FSR}{FWHM} \tag{5.22}$$

the FSR is the free spectral range of the cavity, or the spacing between resonance frequencies and the FWHM is the full width at half maximum or linewidth of the resonances. The higher the finesse of a cavity, the lower the losses and the greater the intra-cavity field strength.

5.3.2 Model of OPO squeezer

In this section we produce a plot which will provide insight into whether a singly resonant or a doubly resonant cavity will ideally be more suitable to the production of highly squeezed states. In the bow-tie cavity which was constructed, the pump beam had one entry and exit port, hence it had a single input/output coupler. For the fundamental, this same mirror is also the output coupler. We produce a contour plot which has the reflectivity of the fundamental on this mirror along the x-axis and the reflectivity of the pump along the y-axis. With this it is possible to determine the ideal reflectivities for this input/output coupler.

We begin by recalling the full quantum description of the cavity equations with the addition of terms that represent the nonlinear coupling between the two modes.

$$\begin{aligned}\dot{a} &= i\Delta_a a - \kappa_a a + \epsilon a^\dagger b + \sqrt{2\kappa^a_{in}}A_{in} + \sqrt{2\kappa^a_{out}}\delta A_{vac} + \sqrt{2\kappa^a_{loss}}\delta A_{loss} \\ \dot{b} &= i\Delta_b b - \kappa_b b - \frac{\epsilon}{2}a^2 + \sqrt{2\kappa^b_{in}}B_{in} + \sqrt{2\kappa^b_{out}}\delta B_{vac} + \sqrt{2\kappa^b_{loss}}\delta B_{loss}\end{aligned} \tag{5.23}$$

The standard method for solving these equations in the singly resonant case is to make two assumptions, both of which are valid in the case of a low finesse cavity for the pump beam, b. The first assumption is that the pump field is a classical field and does not undergo depletion. This assumes that the power in the mode b is not affected by the nonlinear process. Mathematically this means that the full quantum cavity equations, equations 5.23, will have the $\frac{\epsilon}{2}a^2$ term removed. Having a low finesse for the pump beam also allows for the adiabatic elimination of this field. This implies that the pump field acts like a constant on time scales characteristic of the signal field and allows one to set $\dot{b} = 0$. This is equivalent to saying that the cavity is singly resonant with the fundamental frequency, or equivalently, the pump field has its total decay rate much higher than the total decay rate of the fundamental,$\kappa_b \gg \kappa_a$. These assumptions are certainly not valid for the plot we wish to produce as we need to find a solution for doubly and singly resonant cavities, a new approach needs to be undertaken.

In order to produce the desired plot, the first assumption will be that we have no frequency mismatches and hence set $\Delta_a = \Delta_b = 0$. We use many of the conclusions found in Drummond's paper [25] regarding semiclassical sub/second harmonic generation to investigate the stability of the model. One assumption we shall make is that the intra-cavity fields for the seed and the pump, a^0 and b^0 respectively, are purely real. The validity of this assumption may be found in Drummond's paper, where it was shown that with two coherent driving fields, a bistability may arise and hence there may be more than one solution for the fundamental intra-cavity field a. However, we show that under the right operating conditions, this regime can be avoided and the assumption we wish to make about the intra-cavity fields is valid. We assume that we are operating the cavity with below threshold power. Threshold power, P_{th} is defined as

$$P_{th} = \frac{\kappa_a \kappa_b}{\epsilon} \tag{5.24}$$

Below threshold only one in-phase solution exists, and we use this to greatly simplify the situation. The fact that there is only one in-phase solution means that the phase of any input fields will be preserved in the parametric process. If we only wish to look at the cases of either maximum amplification or de-amplification, then we can always find a frame of reference where the two input fields are purely real. If the two input fields are real and phase is preserved then the intra-cavity fields must also be real. Hence we may assume that a^0 and b^0 are purely real if we are operating the system in amplification or deamplification and only below threshold.

The values of a^0 and b^0 can be found from Drummond's paper by solving the steady state relationship between the intra-cavity fields

$$a^0 = \frac{1}{\kappa_a}\left[A_{in} + \epsilon a^{0^*} b^0\right] \tag{5.25}$$

$$b^0 = \frac{1}{\kappa_b}\left[B_{in} - \frac{\epsilon}{2}\left(a^0\right)^2\right] \tag{5.26}$$

and using the only real solution for operation in the below threshold regime.

We then set out to determine the eigenvalues of these equations in order to analyze the behavior of the solutions we obtain. We can follow the same method as that used by Drummond *et al* to obtain the same eigenvalues, λ_k [25],

$$\begin{aligned}\lambda_1, \lambda_2 &= -\frac{1}{2}[- \mid \epsilon b^0 \mid + \kappa_a + \kappa_b] \pm \frac{1}{2}[(- \mid \epsilon b^0 \mid + \kappa_a - \kappa_b)^2 - 4 \mid \epsilon a^0 \mid^2]^{\frac{1}{2}} \\ \lambda_3, \lambda_4 &= -\frac{1}{2}[\mid \epsilon b^0 \mid + \kappa_a + \kappa_b] \pm \frac{1}{2}[(\mid \epsilon b^0 \mid + \kappa_a - \kappa_b)^2 - 4 \mid \epsilon a^0 \mid^2]^{\frac{1}{2}}\end{aligned} \tag{5.27}$$

As for the noise treatment of the empty cavity, the first step towards a solution for the equations is to linearize the fields about their steady states and remove constant terms and terms of second order fluctuations to find

$$\delta\dot{a} = -\kappa_a \delta a + \epsilon a^{0\dagger}\delta b + \epsilon b^0 \delta a^\dagger \sqrt{2\kappa^a_{in}}\delta A_{in} + \sqrt{2\kappa^a_{out}}\delta A_{vac} + \sqrt{2\kappa^a_{loss}}\delta A_{loss} \tag{5.28}$$

$$\delta\dot{b} = -\kappa_b \delta b - \epsilon a^0 \delta a + \sqrt{2\kappa^b_{in}}\delta B_{in} + \sqrt{2\kappa^b_{out}}\delta B_{vac} + \sqrt{2\kappa^b_{loss}}\delta B_{loss} \tag{5.29}$$

The next step uses the assumption that the intra-cavity fields are real. We also make use of the definition of the amplitude quadrature operator $\delta X^+_a = \delta a + \delta a^\dagger$ and after some simplification arrive at

$$\begin{aligned}\delta\dot{X}^+_a &= -\kappa_a \delta X^+_a + \epsilon a^0 \delta X^+_b + \epsilon b^0 \delta X^+_a + \sqrt{2\kappa^a_{in}}\delta X^+_{Ain} + \sqrt{2\kappa^a_{out}}\delta X^+_{Avac} + \sqrt{2\kappa^a_{loss}}\delta X^+_{Aloss} \\ \delta\dot{X}^+_b &= -\kappa_b \delta X^+_b - \epsilon a^0 \delta X^+_a + \sqrt{2\kappa^b_{in}}\delta X^+_{Bin} + \sqrt{2\kappa^b_{out}}\delta X^+_{Bvac} + \sqrt{2\kappa^b_{loss}}\delta X^+_{Bloss}\end{aligned} \tag{5.30}$$

Taking the Fourier transform of these two equations will then place the equations in the frequency domain. Doing so yields

$$\begin{aligned}i\omega\delta\tilde{X}^+_a &= -\kappa_a \delta\tilde{X}^+_a + \epsilon a^0 \delta\tilde{X}^+_b + \epsilon b^0 \delta\tilde{X}^+_a + \sqrt{2\kappa^a_{in}}\delta\tilde{X}^+_{Ain} + \sqrt{2\kappa^a_{out}}\delta\tilde{X}^+_{Avac} + \sqrt{2\kappa^a_{loss}}\delta\tilde{X}^+_{Aloss} \\ i\omega\delta\tilde{X}^+_b &= -\kappa_b \delta\tilde{X}^+_b - \epsilon a^0 \delta\tilde{X}^+_a + \sqrt{2\kappa^b_{in}}\delta\tilde{X}^+_{Bin} + \sqrt{2\kappa^b_{out}}\delta\tilde{X}^+_{Bvac} + \sqrt{2\kappa^b_{loss}}\delta\tilde{X}^+_{Bloss}\end{aligned} \tag{5.31}$$

Simplifying and rearranging we find

$$\begin{pmatrix} \delta\tilde{X}^+_{Ain} \\ \delta\tilde{X}^+_{Bin} \end{pmatrix} = \begin{pmatrix} \frac{i\omega+\kappa_a-\epsilon b^0}{\sqrt{2\kappa^a_{in}}} & \frac{-\epsilon a^0}{\sqrt{2\kappa^a_{in}}} \\ \frac{\epsilon a^0}{\sqrt{2\kappa^b_{in}}} & \frac{i\omega\kappa_b}{\sqrt{2\kappa^b_{in}}} \end{pmatrix} \begin{pmatrix} \delta\tilde{X}^+_a \\ \delta\tilde{X}^+_b \end{pmatrix} - \begin{pmatrix} \frac{\sqrt{2\kappa^a_{out}}}{\sqrt{2\kappa^a_{in}}}\delta\tilde{X}^+_{Avac} & \frac{\sqrt{2\kappa^a_{loss}}}{\sqrt{2\kappa^a_{in}}}\delta\tilde{X}^+_{Aloss} \\ \frac{\sqrt{2\kappa^b_{out}}}{\sqrt{2\kappa^b_{in}}}\delta\tilde{X}^+_{Bvac} & \frac{\sqrt{2\kappa^b_{loss}}}{\sqrt{2\kappa^b_{in}}}\delta\tilde{X}^+_{Bloss} \end{pmatrix} \quad (5.32)$$

which we can now solve for the intra-cavity fields $\delta\tilde{X}^+_a$ and $\delta\tilde{X}^+_b$ and use the cavity input/output relation given by equation 5.3 to obtain

$$\begin{aligned} \delta\tilde{X}^+_{Aout} = & \frac{2\sqrt{\kappa^a_{in}\kappa^a_{out}}(\kappa_b+i\omega)}{a^{0^2}\epsilon^2-(b^0\epsilon-\kappa_a-i\omega)(\kappa_b+i\omega)} \times \\ & (\delta\tilde{X}^+_{Ain} + \left(\frac{\sqrt{\kappa^a_{out}}}{\sqrt{\kappa^a_{in}}} - \left(a^{0^2}\epsilon^2 - \left(b^0\epsilon-\kappa_a-i\omega\right)\left(\kappa_b+i\omega\right)\right)\right)\delta\tilde{X}^+_{Avac} \\ & + \frac{\sqrt{\kappa^a_{loss}}}{\sqrt{\kappa^a_{in}}}\delta\tilde{X}^+_{Aloss}) + \frac{2a^0\epsilon\sqrt{\kappa^b_{in}\kappa^a_{out}}}{a^{0^2}\epsilon^2-(b^0\epsilon-\kappa_a-i\omega)(\kappa_b+i\omega)} \times \\ & \left(\delta\tilde{X}^+_{Bin} + \frac{\sqrt{\kappa^b_{out}}}{\sqrt{\kappa^b_{in}}}\delta\tilde{X}^+_{Bvac} + \frac{\sqrt{\kappa^b_{loss}}}{\sqrt{\kappa^b_{in}}}\delta\tilde{X}^+_{Bloss}\right) \end{aligned} \quad (5.33)$$

Now that we have determined the fluctuations in the amplitude quadrature, we calculate the output variance using equation 5.17.

$$\begin{aligned} V^+_{Aout} = & (a^{0^4}\epsilon^4 + 2a^{0^2}\epsilon^2\left(-b^0\epsilon\kappa_b+\kappa_a\kappa_b+\kappa^a_{out}\left(-2\kappa_b+2\left(\kappa^b_{loss}+\kappa^b_{out}\right)+\kappa^b_{in}V_{Bin}\right)-\omega^2\right) \\ & + \left(\kappa_b^2+\omega^2\right)\left(b^{0^2}\epsilon^2+\kappa_a^2-2b^0\epsilon\left(\kappa_a-2\kappa^a_{out}\right)-4\kappa_a\kappa^a_{out}\right. \\ & \left.+4\kappa^a_{out}\left(\kappa^a_{loss}+\kappa^a_{out}+\kappa^a_{in}V_{Ain}\right)+\omega^2\right))/ \quad (5.34) \\ & \left(a^{0^4}\epsilon^4 - 2a^{0^2}\epsilon^2\left(b^0\epsilon\kappa_b-\kappa_a\kappa_b+\omega^2\right)+\left(\left(-b^0\epsilon+\kappa_a\right)^2+\omega^2\right)\left(\kappa_b^2+\omega^2\right)\right) \quad (5.35) \end{aligned}$$

We can check that this equation is valid for a singly resonant cavity by reapplying the two assumptions generally used to solve the singly resonant case, that the pump field is not depleted and that it can be adiabatically eliminated. To do this we need to remove the term which represents depletion of the pump field from equation 5.23, $-\frac{\epsilon}{2}a^2$, and set all of the cavity decay rates for the pump field as zero, effectively making the pump field single pass. Doing so will yield

$$V^+_{Aout} = 1 + \frac{4\kappa^a_{out}\left(b^0\epsilon-\kappa_a+\kappa^a_{loss}+\kappa^a_{loss}+\kappa^a_{out}+\kappa^a_{in}V_{Ain}\right)}{\left(\kappa_a-b^0\epsilon\right)^2+\omega^2} \quad (5.36)$$

Which is exactly what has been previously calculated [9] for the singly resonant cavity.

5.3.3 Investigation of model and parameters

We are now ready to investigate different features of the model but first it is worthwhile to discuss the assumptions and chosen values. The most limiting assumption that has been made is that the mean field approximation holds. The accuracy of the solution will therefore reduce as the reflectivities approach zero, but as shown by White [12], should still provide reasonable solutions. The model will also break down above threshold, because

in this region out-of-phase solutions may exist and the assumption that the intra-cavity fields are real is invalid.

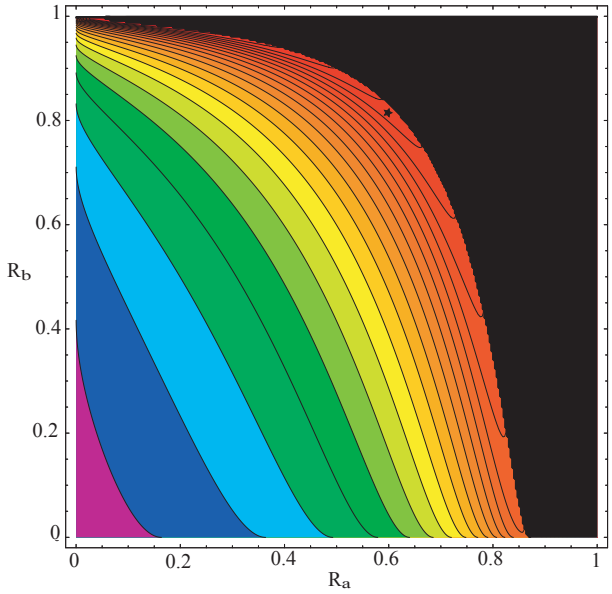

Figure 5.4: PPKTP OPO squeezing model with an input pump power of 500mW. R_a is the reflectivity of the output coupler for the fundamental and R_b is the reflectivity of the input/output coupler for the pump. Each contour depicts a change in squeezing of 1dB. At the star, a theoretical squeezing level of 19dB is found.

Using the analytical Boyd-Kleinman method [26, 27] we can find an approximation to the value of the nonlinear coupling coefficient, ϵ. To calculate this value is nontrivial as it depends upon many experimental factors such as beam waist size, crystal length, and will also be affected by the properties of the crystal such as the second order nonlinearity coefficient and the quality of the poling domains within. The values of the second order nonlinearity and the lengths of the crystals were stated in chapter 4. The cavity was designed so to have a waist of approximately 38μm. The optimum Boyd-Kleinmann waist size was smaller than this, at approximately 25μm as previously calculated [28], however, the larger waist was the closest that this particular bow-tie cavity could produce before problems were expected to arise. One factor was that in order to keep the bow-tie compact the spacing between the flat mirrors could not become too large in order to keep the bow-tie compact, and it also had to be ensured that the beam bouncing off one of the curved mirrors would not clip the other mirror on its way to the other side of the cavity. By having a larger waist size, and hence curved mirrors of longer focal length, it was also hoped that abberation could be avoided. It will be necessary to multiply the $\chi^{(2)}$ values by a factor, $\frac{2}{\pi}$, which is due to the reduction in the effective second order nonlinearity caused by the periodic poling of the material, as shown in equation 3.11. Doing so yields ϵ values of 4180 $s^{-\frac{1}{2}}$, 2394 $s^{-\frac{1}{2}}$ and 2312 $s^{-\frac{1}{2}}$ for PPMgO:SLN, PPSLT and PPKTP respectively.

The bow-tie cavity used in this thesis was the model for the plots, the length of the cavity was taken to be 0.33 metres, the reflectivities of the 3 mirrors which were not the input/output coupler for the pump were 99.9% for the signal frequency and 99.85% for the pump frequency. The highest levels of squeezing in the experiment were found to be

at a sideband frequency of 2MHz and as such this is the observation frequency used in the plots. Also assumed was that the input fields for the seed and the pump were coherent states. The power of these input fields could be altered to simulate an OPA or an OPO with differing input powers. Loss due to transmission through the nonlinear mediums was estimated to be 0.1% at each surface at 1064nm and 0.2% per surface at 532nm. Loss due to absorption and scattering in the crystal was estimated at 0.5% per centimetre for 1064nm and 2% at 532nm. Using these values we are able to obtain a plot for each of the nonlinear materials. The black region in the plots signifies that the system has entered the above threshold regime and the contour lines are chosen to represent a change of 1dB in the squeezing. As a reference, the light blue region indicates that a squeezing between 3 to 4dB is theoretically produced.

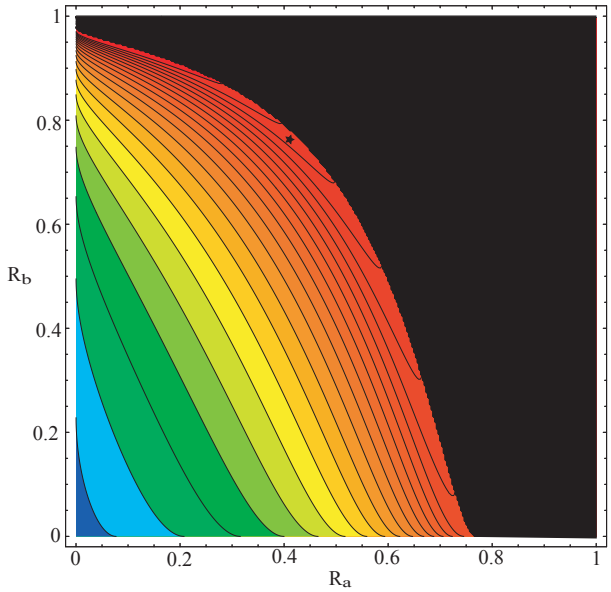

Figure 5.5: MgO:PPSLN OPO squeezing model with an input pump power of 500mW. R_a is the reflectivity of the output coupler for the fundamental and R_b is the reflectivity of the input/output coupler for the pump. Each contour depicts a change in squeezing of 1dB. At the star, a theoretical squeezing level of 21dB is found.

As is certainly not surprising, the MgO:PPSLN is theoretically able to achieve better squeezing due to its stronger second order nonlinearity. Another advantage is that threshold is reached much earlier than for the PPSLT or PPKTP. This will reduce the intra-cavity powers needed to achieve high levels of squeezing and hence the chance of damaging optics or the nonlinear material itself is reduced. Higher powers can also heat optics through the photothermal effect and this may adversely affect the stability of the experiment. Not surprisingly, the plots for the PPKTP and the PPSLT are very similar, on account of them having nearly identical second order nonlinearities. General trends from all three plots is that the closer we are to threshold, the better the squeezing we can expect to see. Also, the lower the reflectivity in the fundamental, the stronger the squeezing. This can be explored through the introduction of a variable known as the escape efficiency

$$\eta_{esc} = \frac{\kappa^a_{out}}{\kappa_a} \tag{5.37}$$

The escape efficiency quantifies the amount of light at the seed frequency which will exit the cavity at the output coupler. Maximising the escape efficiency, by moving towards a system which is resonant at 532nm, comes at a cost, because it is evident that as we move the operating region along the line of threshold towards a system resonant at the pump mode, the stability of the squeezing is also reduced, which is indicated by the closely spaced contour lines in this region on the plots. In this region, roughly R_a from 0 to 0.4 and R_b from 0.9 and above, small fluctuations in the pump power will be enough to drastically affect the squeezing and may even put the system above threshold. This is shown in figures 5.7 to 5.10, which indicate that changes in the pump power will affect the boundary where threshold occurs. By increasing the reflectivity of the input/output coupler at 532nm we are also increasing the strength of the intra-cavity field significantly and this may become a problem for high input powers. The stars have been added to the figures to indicate possible operating regimes which are stable and will produce high levels of squeezing. Reducing the reflectivity of the fundamental and increasing the reflectivity of the pump past this point will improve the squeezing but reduce the stability of the system. A system which is singly resonant in the second harmonic will achieve the highest levels of squeezing but will be sensitive to fluctuations in the pump power, also the intra-cavity powers will increase and photorefractive damage and other photothermal effects may become a serious problem.

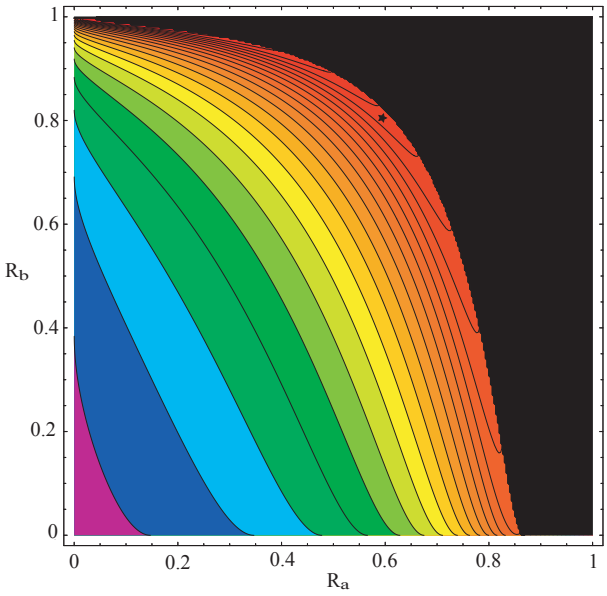

Figure 5.6: PPSLT OPO squeezing model with an input pump power of 500mW. R_a is the reflectivity of the output coupler for the fundamental and R_b is the reflectivity of the input/output coupler for the pump. Each contour depicts a change in squeezing of 1dB. At the star, a theoretical squeezing level of 19dB is found.

5.3.4 Increasing pump power

The first system parameter we investigate is the pump power. For PPKTP we produce 4 plots with parameters equal to those in figures 5.4, 5.6 and 5.5 but with increasing input pump powers. In order to make it easier to determine if damage will be a problem, the finesse of the cavity at the optimum operating conditions indicated by the stars is also calculated. The circulating power inside the cavity can be estimated as the input power multiplied by the finesse of the cavity. The loss due to the PPKTP crystal is calculated in chapter 8 for 1064nm as 0.9% in total, and we will assume that the losses at 532nm are twice that at 1064nm.

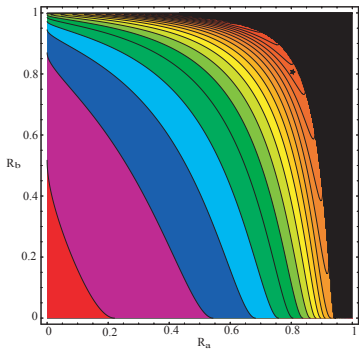

Figure 5.7: PPKTP OPO setup with 100mW pump. At the star a theoretical squeezing of 15dB is found and the cavity has a finesse of 8 and 4 at 1064nm and 532nm respectively.

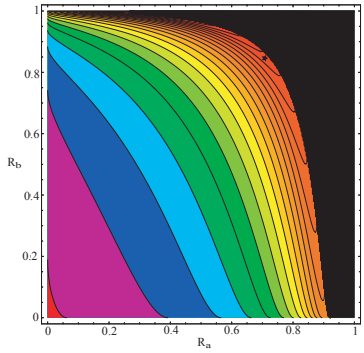

Figure 5.8: PPKTP OPO setup with 200mW pump. At the star a theoretical squeezing of 17dB is found and the cavity has a finesse of 7 and 4 at 1064nm and 532nm respectively.

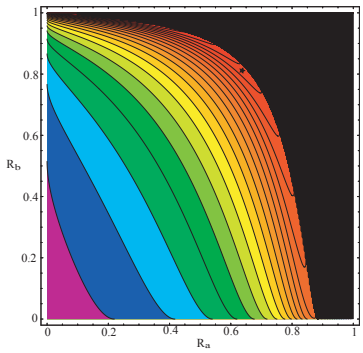

Figure 5.9: PPKTP OPO setup with 400mW pump. At the star a theoretical squeezing of 18dB is found and the cavity has a finesse of 6 and 4 at 1064nm and 532nm respectively.

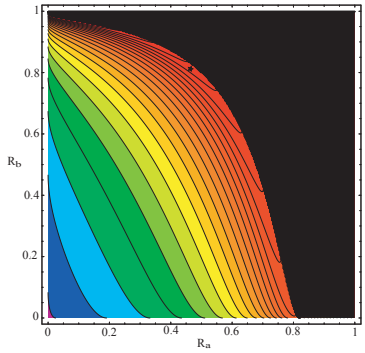

Figure 5.10: PPKTP OPO setup with 1000mW pump. At the star a theoretical squeezing of 20dB is found and the cavity has a finesse of 5 and 4 at 1064nm and 532nm respectively.

From the figures we notice a number of effects. Not surprisingly, the threshold region occurs at lower mirror reflectivities with higher pump powers. Not so obvious, however, is the fact that the loss in squeezing, seen by having a lower pump power, can't be compensated for by altering the mirror reflectivities, as the squeezing is still reduced compared to the values which may be observed with a higher pump power. This can be explained in terms of the escape efficiency. With a higher pump power, threshold occurs earlier on the

plot and this implies that the reflectivity at the seed frequency is reduced. By reducing the reflectivity at which threshold occurs, we have improved the escape efficiency and this is why we expect to see more squeezing with these higher powers. There will be a limit to the amount of power we can put into the cavity, as high powers may introduce new effects which will reduce the squeezing, such as photorefractive damage, photothermal effects and perhaps for some of the materials, green induced infra-red absorption (GRIIRA) [17] or thermal lensing. From these figures we also note that the contour lines at the top of the figures ,the case of a cavity singly resonant at the pump frequency, begin to spread as pump powers are increased. This means that at higher pump powers, fluctuations in the intensity of the pump are going to affect the squeezing less than they would for a lower power. Not only does a higher pump power increase the observed squeezing but for the strongest squeezing, it also improves the stability if thermal effects are overcome. The best squeezing will be found where the input pump powers are close to threshold and also as high as possible without introducing unwanted photothermal effects.

5.3.5 Intra-cavity losses

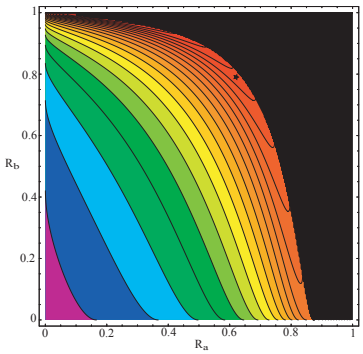

Figure 5.11: PPKTP OPO setup with intra-cavity losses of 0.3% at 1064nm and 0.4% at 532nm. At the star a theoretical squeezing of 17dB is found.

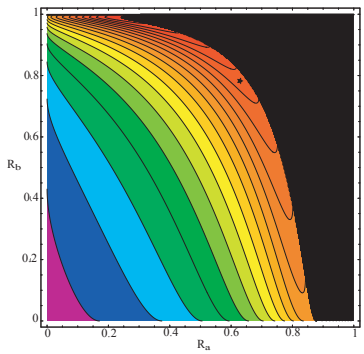

Figure 5.12: PPKTP OPO setup with intra-cavity losses of 0.7% at 1064nm and 1.2% at 532nm. At the star a theoretical squeezing of 15dB is found.

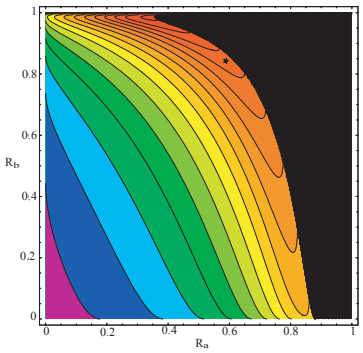

Figure 5.13: PPKTP OPO setup with intra-cavity losses of 1.2% at 1064nm and 2.2% at 532nm. At the star a theoretical squeezing of 13dB is found.

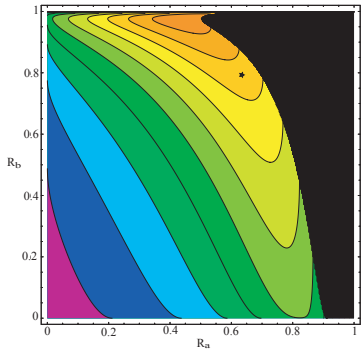

Figure 5.14: PPKTP OPO setup with intra-cavity losses of 4.2% at 1064nm and 4.2% at 532nm. At the star a theoretical squeezing of 9dB is found.

Now we investigate the effect of intra-cavity losses on the expected squeezing, designed to mimic the loss introduced by transmission through one of the nonlinear crystals. For an OPO setup with PPKTP as the nonlinear medium and 500mW pump, we vary the loss inside the cavity to simulate the effect that an imperfect crystal has on the model. The losses are generally higher for 532nm than they are for 1064nm and the values have been chosen to represent this.

Figures 5.11 to 5.14 make it incredibly obvious that intra-cavity losses will have a very strong negative impact on the expected squeezing. The crystal will introduce two sources of loss, losses internal to the crystal due to scattering or absorption, as well as the losses from the two anti-reflection coated surfaces. This makes it apparent that the anti-reflection coatings on the crystal are imperative to producing high levels of squeezing. The loss through the crystal due to scattering and absorption is harder to reduce, stoichiometric growths may reduce the loss because there will be less defects to scatter from. In the figures, the values have been chosen to emulate losses due to the nonlinear medium but poor cavity mirrors or other sources of loss such as dust on a mirror surface will have the same effect. Comparing the almost lossless case shown in figure 5.11 to figure 5.13, we might expect to see a reduction in squeezing of approximately 4dB due to an increase in the intra-cavity loss of only 0.9% and 1.8% at 1064nm and 532nm respectively. Keeping the intra-cavity losses to a minimum is essential in obtaining strong squeezing, all anti-reflection coatings are very important and care must be taken when constructing the cavity.

Experimental Design

6.1 Experimental layout

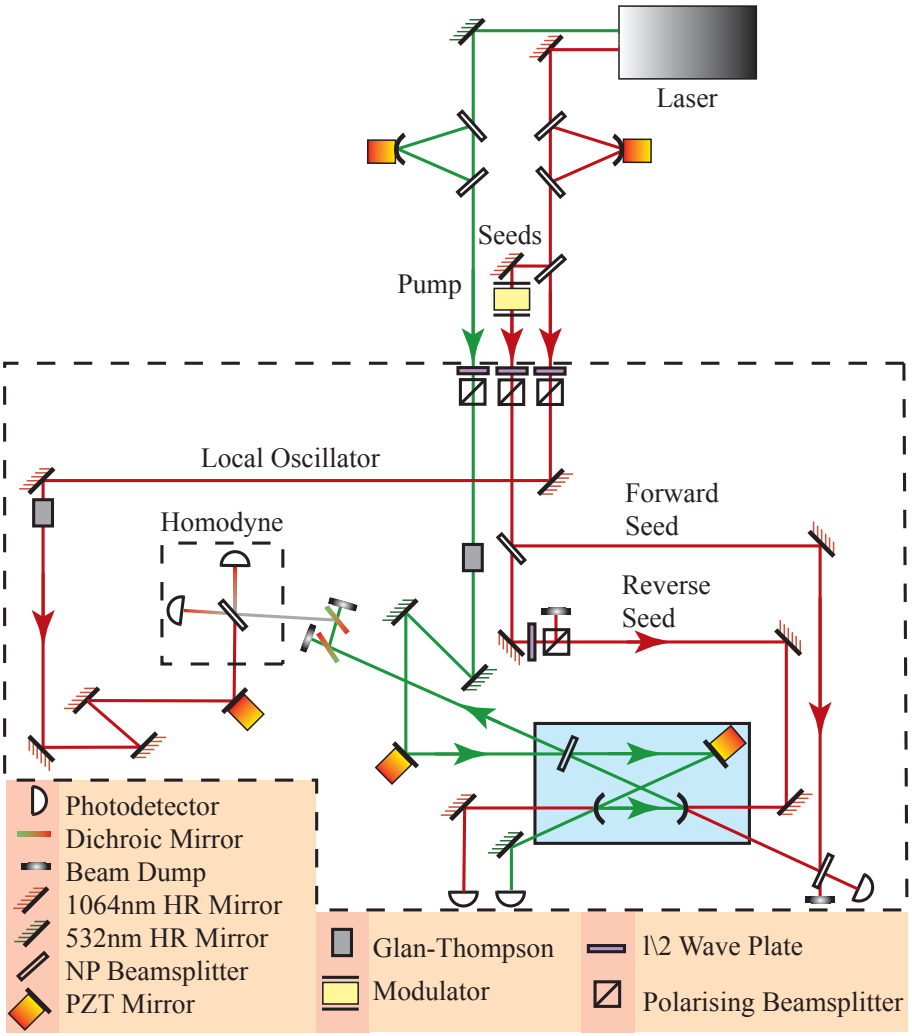

Figure 6.1: Experimental design. The dashed box indicates the part of the experiment constructed for this thesis. The mode cleaner cavities and laser were previously setup [28] for another experiment and power from these modecleaners were split to both experiments. Mode matching lenses are not shown.

6.2 Design considerations for high level squeezing

In trying to explore methods for reaching high levels of squeezing, it is important to examine which factors are going to affect the outcome of the experiment. It is useful to separate the issues of production of a squeezed state and the detection of the squeezed state. In producing the squeezed beam in an OPA/OPO experiment, perhaps the most obvious system parameter that we wish to enhance is the strength of the nonlinear coupling, ϵ. This is affected by parameters such as the strength of the second order nonlinearity, the waist size, the length of the nonlinear medium and the intra-cavity losses. The effective nonlinear coupling is also affected by second order effects such as phase matching, which is in turn affected by the stability of the temperature control of the crystal. Every component in the experiment needs to be carefully chosen and tailored to its specific application.

Once a source of squeezed light has been produced, it is still a challenge to measure that squeezing. Any loss on a squeezed beam will introduce vacuum fluctuations into the squeezed beam. This means that upon detection, the maximum detectable squeezing is reduced since the introduction of vacuum fluctuations to the squeezed state results in the properties of the squeezed state approaching the properties of a vacuum.

6.3 Components

6.3.1 Laser

In this experiment a Diabolo Nd:YAG laser from Innolight is the source of the 1064nm fundamental light. These lasers are incredibly stable and as such the frequency of the laser is chosen as the reference for all locking loops. This means that any cavities in the experiment are tuned to the laser, not the opposite. The diabolo has a frequency doubler in it which was able to output in excess of 900mW of power at 532nm and produced over 350mW of power at 1064nm. The laser had a relaxation oscillation at approximately 1MHz as shown in Figure 7.1, but also had a noise eater to greatly reduce the magnitude of this noise source. The noise eater coupled with the common mode rejection of the homodyne detector, which was upwards of 35dB rejection, resulted in almost complete removal of the relaxation oscillation from the spectrum.

6.3.2 Mode cleaner

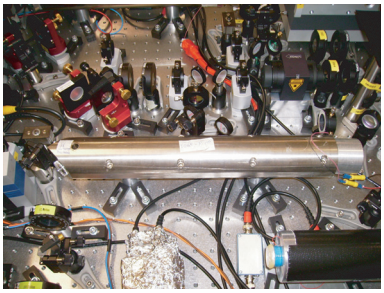

Figure 6.2: Mode cleaner used in the experiment.

The effects of the mode cleaner cavity were discussed in chapter 5. It was shown that

a mode cleaner acted as a low pass filter as well as a spatial mode filter. Mode cleaner cavities were added to both the 1064nm fundamental beam and the 532nm pump beam to achieve both of these effects. The mode cleaners are three mirror ring cavities. Note that their round trip time is maximised by increasing the length of the cavities so as to reduce the free spectral range, which will give a smaller cavity linewidth. The linewidth of the 532nm mode cleaner was approximately 400kHz and the linewidth of the 1064nm mode cleaner was approximately 220kHz.

6.3.3 Bow-tie cavity

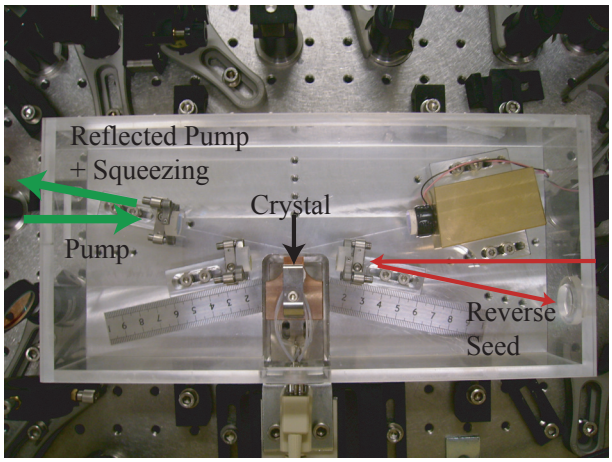

Figure 6.3: Bow-tie cavity used in the experiment.

The major strength of the bow-tie cavity for this experiment, is the ease it affords when replacing nonlinear crystals. Once the experiment was aligned with one of the crystals in place, it was possible to replace the crystal with another and have the experiment producing squeezing again in only one day. Perhaps the only disadvantage with the bow-tie cavity is the addition of mirrors which would not be present in say, a linear cavity design. These additional mirrors will introduce extra sources of intra-cavity losses, which can obviously be reduced by using very highly reflective mirrors, but not without a cost. Another advantage to the bow-tie cavity is the forward and reverse seeding options it affords which are not available with standing-wave designs.

6.3.4 Input/output coupler

The input/output coupler used had a specified reflectivity of 90% for 1064nm and 40% for 532nm. Previous tests [28] on another coupler with the same specifications revealed that the reflectivity at 1064nm was closer to 93% and at 532nm was closer to 50%. The plots in chapter 5 indicate that more squeezing might be expected if the reflectivity of the coupler for 1064nm were reduced and the reflectivity at 532nm was increased accordingly, thereby moving towards a more doubly resonant system. This coupler was the best available at the time, for which the model produced in chapter 5 predicted the highest levels of squeezing.

6.3.5 Seeding options

The bow-tie cavity allows for front and back seeding in the forward and the reverse directions. Front seeding is defined as the case where the fundamental enters the cavity at the same mirror as the pump beam, whilst back seeding implies that the fundamental enters on any of the other mirrors. A forward direction fundamental propagates in the same direction as the pump within the cavity and hence will act as a seed to create an OPA setup. A reverse direction seed propagates in the opposite direction to the pump and therefore will theoretically not undergo any nonlinear process. The setup chosen for this experiment is shown in Figures 5.2 and 6.1. Originally, a forward direction seed entering from the rear curved mirror was to be chosen as the source of the error signal for the lock and hence a DOPA was to be built. The problem was that the phase of the pump was seen to affect the error signal, by introducing a DC offset as the phase was varied. The DC offset would affect the lock by shifting the zero crossing and this would introduce a phase-jitter, discussed in the following section, which has the effect of reducing the observable squeezing. For this reason, the reverse direction seed was chosen instead. The forward direction seed was still present in the experiment, though was blocked for all squeezing runs and its main purpose was for alignment of the homodyne detector.

With the reverse direction seed in place, the cavity was now ideally an OPO, with a 1064nm error signal exiting the rear of the cavity. Another advantage with the OPO setup is that there is no seed to add extra noise to the system, and the lack of a seed removes, to first order, noise from the pump and noise from cavity detuning [14]. A lock to the 1064nm seed was favoured over using the 532nm pump to lock because the finesse of the cavity was higher at 1064nm and this improves the error signal by increasing the gradient of the line that crosses zero on resonance. Increasing the gradient will provide a more sensitive lock because the magnitude of the feedback voltage will be larger for a given offset from resonance. With the 1064nm locked, a co-resonance condition can be found for the flat crystals, by varying the temperature of the crystal because the dispersion due to the crystal will vary.

6.3.6 Electronics

The stability of an experiment is influenced greatly by the quality of the electronics controlling the locks. For example, if the lock of the bow-tie cavity is oscillating at a high frequency, then one of the effects this will have is that the squeezing ellipse from the ball on stick picture will rotate, because the reflected and transmitted carriers will pick up a phase shift as the cavity moves on and off resonance. If the frequency is so high that electronics further down the detection loop cannot resolve the oscillations, then an average of the motion will be detected and this will reduce the observed squeezing. This case is shown in figure 6.4, note that the projection onto the X^{θ} quadrature of what was once a highly squeezed state for this detection angle, is now broadened. It is important to ensure a stable lock so that this effect, known as phase-jitter, is avoided.

6.3.7 PDH locking

Pound-Drever-Hall locking provides an error signal for locking the cavities in the experiment to the frequency of the laser, which is independent of fluctuations in the intensity of the laser. PDH locking requires that the light entering the cavity be phase modulated and works in two regimes. The first regime is for sidebands, which are well inside the

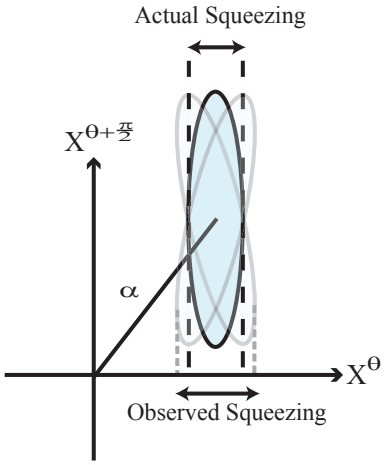

Figure 6.4: An oscillating squeezing ellipse. If the rotations due to an oscillating phase shift are fast enough that the electronics cannot resolve the oscillations, then the rotations are averaged and the observed squeezing is less than the actual squeezing present. This effect becomes more apparent as the squeezing is increased and the ellipse becomes elongated to a higher degree.

cavity linewidth. When off resonance the cavity will impart a differential attenuation to the two sidebands which will produce an AM component from the original PM input. On resonance there is no differential attenuation of the sidebands and hence no AM output. Therefore, we have a zero crossing on resonance and the polarity and magnitude of the AM component when off resonance will indicate how far off resonance we are, as well as the direction we need to go in order to reach resonance. This information is sent to the piezoelectric transducer (PZT) on one of the cavity mirrors to change the length of the cavity, after mixing and low pass filtering. The PDH lock was chosen in this experiment over other methods such as dither locking or tilt locking for a couple of reasons. In PDH locking the size of the error signal can be easily increased by increasing the modulation depth of the light and is generally the most stable lock. Particularly for the OPO cavity, the quality of the lock is essential to producing a stable source of squeezing and it makes sense to choose the lock which offers the strongest error signal. A possible negative effect of PDH locking, is that it will allow some of the modulation sidebands to travel through the cavity and hence will introduce noise at the frequency of modulation for low to moderate finesse cavities. However, the modulation frequency is chosen such that it is well outside the linewidth of the cavity and as such will not interfere with measurements of squeezing for this experiment. Dither locking on the other hand, will introduce a phase modulation within the linewidth of the cavity and hence will affect squeezing measurements around these frequencies and will become a problem if one wishes to detect low frequency squeezing.

The other regime for PDH locking, the one used in the experiment, involves modulating the light well outside the linewidth of the cavity. In this regime, when off resonance the carrier will experience a phase shift. This phase shift will again convert some of the original PM into AM and will indicate the direction that resonance is and the magnitude of the mismatch. The error signal obtained from the PDH locking scheme for a cavity with a linewidth of 15MHz and a finesse of 100 is shown in figure 6.5. In order to retrieve the error signal, the output from the photodetector is first mixed with a signal of the same

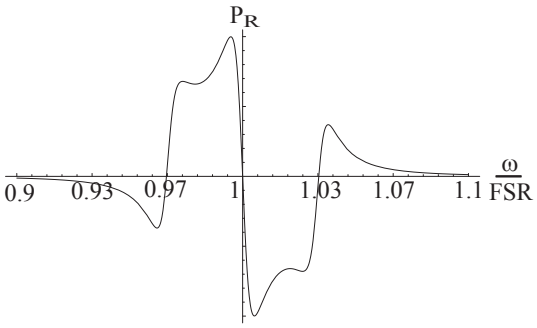

Figure 6.5: Model of a PDH error signal normalized to the free spectral range. The cavity has a finesse of 100, a linewidth of 15MHz and phase modulation at 50MHz. These values are similar to the properties of the bow-tie cavity used in the experiment. P_R is the reflected power from the cavity and the FSR is the free spectral range

frequency as the original phase modulation. The phase of the two signals being mixed must be equal in order to retrieve the desired error signal and this is achieved using lengths of cable. Once the signal has been mixed it is then put through a low pass filter whose cutoff frequency is less than the the frequency of the modulation in order to retain only the DC terms. This is then passed through a proportional-integral-differentiator (PID) unit. A capacitor inside of this unit is used to stabilise the lock and force the resonance condition by increasing the gain at DC. The final stage is to then pass this signal through a high voltage amplifier which is connected to a PZT in the cavity, completing the feedback loop. A schematic for the signal processing is shown in figure 6.6

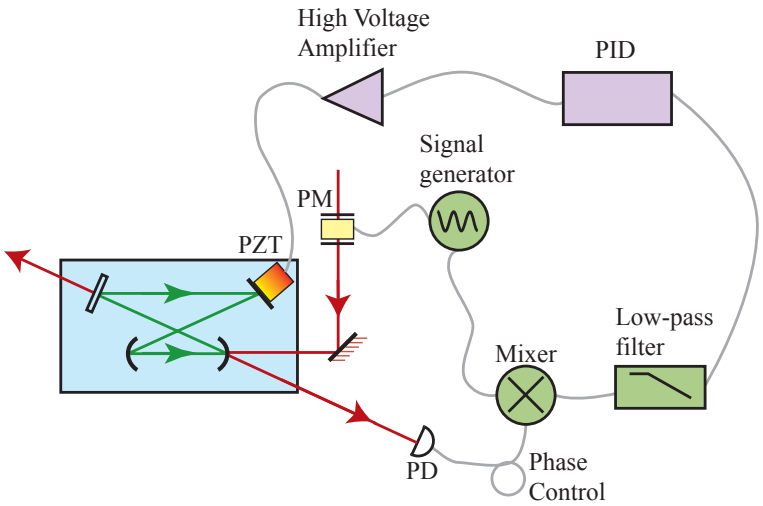

Figure 6.6: Schematic of a PDH lock showing all the important optical and electronic components.

6.4 Detecting the squeezed state

There is no use in producing the most highly squeezed state in history if your apparatus does not allow for the efficient detection of that state. The higher the squeezing that one wishes to detect, the greater the influence that loss has on the measurement. With enough losses, what was once a squeezed state will become a vacuum state. With this in mind, there are a few major elements of this experiment which can be tailored to reduce the loss on the squezed beam and by doing so allow for the detection of high levels of squeezing.

6.4.1 Stability of lock

As shown in figure 6.4, the stability of the phase of the pump can affect the squeezing which is detected. Other issues which can affect the detection of the squeezed state are external noise sources such as sound waves, seismic vibrations and air currents. To reduce noise from seismic vibrations, the table that the experiment is constructed on is a damped optics table from Newport, designed to reduce this noise source. These noise sources, as well as noise from scattered light have a much greater effect at audio frequencies [14].

6.4.2 Homodyne detection

The homodyne detector is the last stage before the optical signal is transferred to an electronic signal and displayed on a spectrum analyser. A homodyne detector is a necessity in order to probe the properties of the squeezed beam, because the vacuum squeezed beam does not have a carrier which we can measure to infer the properties of the state of light. A schematic of a homodyne detector is shown in figure 6.7. A detailed explanation of the mathematics may be found in [29].

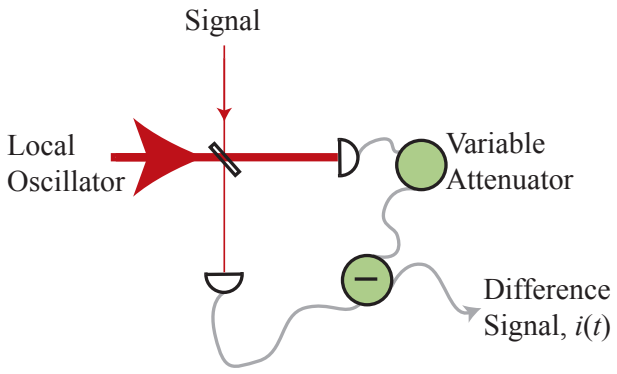

Figure 6.7: Schematic of a homodyne detection scheme. A high intensity local oscillator is mixed on a 50:50 beam splitter with a weak signal.

The difference signal, $i(t)$, depicted in figure 6.7 provides insight as to how the homodyne detector operates and is written

$$i(t) \approx 2\alpha_{LO}\left(\delta X_S^{+} cos\left(\phi_{LO}\right) + \imath\delta X_S^{-} sin\left(\phi_{LO}\right)\right) \tag{6.1}$$

Where subscripts S and LO refer to properties of the signal and local oscillator beams respectively, and ϕ_{LO} refers to the phase of the local oscillator. Calculating the variance

for many frequencies will indicate the trace we would expect to see upon viewing this signal with a spectrum analyser, and is given by

$$\Delta i^2 \approx 4\alpha_{LO}\left(\delta X_S^{+^2} cos^2\left(\phi_{LO}\right) + \delta X_S^{-^2} sin^2\left(\phi_{LO}\right)\right) \tag{6.2}$$

The homodyne detector can be used to measure the noise in the phase or amplitude quadrature and any angle between the two. The mathematics dictates that the power of the local oscillator must be much larger than the power of the signal beam in order to probe the noise properties of the signal. A local oscillator power of 4.5mW was used in this experiment, higher powers were not required as the vacuum squeezed state which was being measured has no coherent amplitude. Note that the noise of the local oscillator ideally does not affect the measurements and that the strength of the signal will scale with the intensity of the local oscillator as shown by equation 6.2.

The hardest task in setting up a homodyne detector is to balance the two beams such that a true 50:50 split is found on the beamsplitter. In theory it is possible to have the two beams undergo perfect destructive interference and hence no power would be present on either of the photodetectors. In practice, however, many parameters will limit the amount of destructive or constructive interference we might see, such as the polarisation of the two beams, their powers, their spatial modes and their spot sizes. By definition, two beams with orthogonal linear polarisations will not interfere and hence it is important that the polarisation of the signal and the local oscillator match. Fine filtering of the local oscillator was done using a Glan-Thompson linear polariser as shown in figure 6.1. Both beams entering the beamsplitter should be Gaussian beams, due to the spatial filtering effects of the mode cleaners, unless effects such as mirror clipping have affected the mode of the light. To get a good spatial overlap it should only be necessary to ensure that the spot sizes are equal at the beam splitter. This is done using a set of lenses inside the path of the local oscillator. Note that the spot size and polarisation of the local oscillator has been matched to the properties of the signal/squeezed beam. This has been done so as not to introduce unnecessary losses into the squeezed beam, which would reduce the squeezing. The visibility, ν, of the homodyne detector is defined as

$$\nu = \frac{I_{max} - I_{min}}{I_{max} + I_{min}} \tag{6.3}$$

where I is the intensity of the beam as seen on one of the photodetectors in the homodyne. The phase of the local oscillator can be varied using the piezo-electric transducer in the path of the local oscillator to scan between the condition for destructive or constructive interference in order to measure the visibility. It is imperative that the visibility is maximised, as poor visibility is equivalent to a beamsplitter with a transmissivity of ν^2, which will introduce losses and hence reduce the squeezing.

Now we investigate methods of improving the electronics in the homodyne. The two signals from each of the photodetectors is fed into a subtractor. This allows for the subtraction of noise which is common to the two photodetectors, as well as the noise of the local oscillator. By doing so we are ideally only left with the noise on the signal beam as indicated by equation 6.2. We can measure the suppression of the unwanted noise sources by noting the difference in the magnitude of a noise source in one of the photodetectors, such as the laser relaxation oscillation, compared with the magnitude of the noise after subtraction. This is called the common mode rejection of the homodyne detector. The two photodetectors will undoubtedly have slightly differing gains. By putting a variable

attenuator of some sort in line with the photodetector which has the higher gain, the common mode rejection can be improved, by matching the magnitude of the two signals entering the subtractor.

Squeezing Results

7.1 Experimental procedure

One of the aims of this experiment was to get a reasonable estimate on the properties of each of the crystals. This required that the procedure was tailored such that the conditions for each of the crystals was essentially the same. Below are the important stages in the experiment and details as to how this aim was achieved.

7.1.1 Inserting crystal

It was a simple matter to swap the crystals in the bow-tie cavity because the design of the cavity allowed for easy modifications [28]. Replacing one crystal with another would generally destabilise the cavity geometry due to the difference in refractive indices of the materials. However, this was easily accounted for through adjustment of the curved mirrors in the bow-tie cavity, shown in figure 5.2, whose spacing could be altered to again reach a stable operating region. As the mirrors were moved and the cavity became unstable, it could be seen that the spot size of the output mode would enlarge quite suddenly. A minimum and a maximum mirror separation, indicating the points of instability, could be found and the cavity was operated in the middle of these two extremes. Some adjustments to the curved mirror mounts inside of the cavity could be made to improve the mode matching of the cavity.

7.1.2 Modematching

Once the crystal had been replaced and the curved mirror mounts adjusted, the mode matching for the pump and two seed beams had to be tweaked using the steering mirrors and lenses. The mode matching of a cavity is defined as the sum of the power in the TEM_{00} mode, divided by the sum of the power in all of the modes which resonate over a full free spectral range.

$$\text{Modematching} = \frac{P_{TEM_{00}}}{P_{TEM_{00}} + \sum P_{othermodes}} \tag{7.1}$$

A cavity with perfect mode matching would have only the TEM_{00} mode resonant, hence only one spike in power would be seen as the cavity length was scanned over one free spectral range. Mode matching of the pump is important to get a reasonable estimate of the threshold power and matching of the reverse seed is important to get a large error signal. The matching of the forward seed however was not so crucial, because it was the transmission being used to align the homodyne detector, which meant that the mode

would be spatially cleaned and hence the only negative effect would be a reduction in power. A change in transmitted power could be adjusted for by reducing the power in the local oscillator arm until it matched the power of the forward seed that reached the homodyne stage.

7.1.3 Locking

With the reverse seed matched back into the cavity, the error signal was recovered. It was previously shown that an unstable lock can have negative effects on the observed squeezing. To provide the most stable lock, the gain of the PID is increased up to a point just before oscillations begin to arise. The offset on the PID is adjusted to ensure that the fluctuations of the locked cavity are at a minimum, which corresponds to a zero detuning of the cavity.

7.1.4 Visibility

After locking the cavity using the reverse seed, the forward seed was opened so that the homodyne detector could be aligned. Slowly scanning the phase of the local oscillator by applying a ramp voltage signal to the PZT just before the homodyne detector, allowed for the measurement of the maximum and minimum intensities on one of the photodetectors. In the experiment, the highest visibility achieved was approximately 98%, which is not ideal as this equates to an almost 4% loss on the squeezing.

7.1.5 Common mode rejection

The final step in enhancing the detection process was to ensure that the common mode rejection was maximised by adjusting the variable attenuator shown in figure 6.7. The attenuator was essentially a switch box with many resistors because it would be phase preserving, used in place of a standard rotating variable resistor which would not preserve the phase. An attenuator which did not preserve the phase would affect the frequency response of the detection. The minimum common mode rejection for the squeezing runs done with any of the crystals was 38dB. The photodiodes used, the ETX500, were recently tested to have a quantum efficiency of 95$\pm$2%.

7.1.6 Method of squeezing optimisation

Obtaining the maximum squeezing with any of the materials required the optimisation of many system parameters. The squeezing tended to increase in all of the crystals the closer the power was to threshold. It was necessary, however, to drop the power to a point where the magnitude of fluctuations in the pump were not expected to push the system above threshold. For this reason the optimum squeezing runs were taken at approximately 94% of threshold. At this power the system was not seen to cross threshold, which in the OPO will be indicated by a sudden production of power at the fundamental. With the pump entering the cavity, the forward direction seed was opened and the length of the bow-tie was scanned by applying a voltage with the profile of a triangle function to the PZT inside the cavity.

The optimum phase matching temperature could be determined by finding the temperature at which maximum OPA gain would occur at this pump power. Introducing the forward direction seed into the cavity, whilst concurrently scanning the phase of the pump

and the length of the cavity, the power at the seed frequency which exited the cavity was seen to undergo amplification and de-amplification. The optimum phase matching temperature was at the point of maximum amplification which was found by varying the temperature of the crystal as the phase of the pump was scanned.

The co-resonance condition had to then be found to determine if this condition would increse the squeezing. For the flat crystals this generally required tuning the temperature slightly off the optimum phase matching condition. This is where the advantage of the wedged material became apparent. The method used to determine co-resonance for the wedged PPSLT is explained in detail in chapter 8. For the flat crystals, the first step was to lock the cavity using the reverse seed and insert the pump. With the homodyne aligned and the phase of the local oscillator scanning at only a few times per second, squeezing could now be detected. By tuning the temperature of the crystal, temperature dependent dispersion would change the resonance condition of the pump, but the cavity would remain on resonance at 1064nm due to the lock provided by the reverse seed. The temperature was varied around what was found to be the optimum phase matching temperature in order to determine if the squeezing could be improved by varying the temperature, and henc the co-resonance condition. The lock of the cavity was then re-calibrated to ensure that the lock on the cavity was as stable as possible. The gain was maximised to ensure a strong lock to resonance and the offset on the PID was set to zero to ensure that the PZT did not oscillate.

7.2 Producing squeezing traces

To find the sideband frequency at which the strongest squeezing occurred, the first plot produced for each crystal consisted of the dark noise, the shot noise and ten squeezing traces. The phase of the local oscillator was scanned for the squeezing traces at a rate of approximately ten times per second. This scan rate could be altered to fit a number of scans of the amplitude and phase quadrature of the squeezed beam in a single trace. Care must be taken to ensure that the scan rate is not too fast, lest the maximum squeezing be lost to averaging from the spectrum analyser as the amplitude quadrature is scanned. These traces, which indicate the squeezing as a function of frequency, were plotted over a span from 300kHz to 15MHz, with a video bandwidth of 30Hz, a sweep time of 2 seconds and a resolution bandwidth of 100kHz.

For the final measurement, a zero frequency span was taken for each crystal, at the frequency where high levels of squeezing were observed on the previous plot. Again the traces had a video bandwidth of 30Hz, a sweep time of 2 seconds and a resolution bandwidth of 100kHz. The phase of the local oscillator was scanned at a rate of approximately 1Hz to ensure that the minimum squeezing was not reduced through averaging. Many traces were recorded with both the pump power and the temperature of the crystal varied each time, in order to reach the strongest squeezing possible with the setup. These traces have been normalised to the shot noise so that the amount of squeezing is clearer, the traces have not had dark noise subtracted.

7.3 Interpreting squeezing traces

There are three important features on the squeezing traces. The dark noise is a measure of the electronic noise of the system, found when no photons are incident on the photode-

tectors. The dark noise will add an offset to any squeezing measurements and may be subtracted from the squeezing traces as well as the dark noise, although in our traces we have opted not to subtract this noise in order to show the squeezing which was directly observed. The shot noise is determined by blocking the squeezed beam and observing the output of the homodyne on the spectrum analyser, it is indicated by a blue line on all of the traces. The squeezing traces are in the shape of arcs because the phase of the local oscillator is being scanned and hence we are probing all angles of the general quadrature operator. The regions where the squeezing trace drops below the shot noise, indicate that the light is squeezed at that angle of the general quadrature operator, determined by the phase of the local oscillator.

7.4 Squeezing results

7.4.1 PPKTP

Figures 7.1 and 7.2 show the results for the PPKTP crystal. The threshold power for the OPO with this crystal in the cavity was approximately 110mW. Squeezing levels of 5.8±0.1dB were directly observed at a frequency of 1.9MHz. This level of squeezing was achieved with an input pump power of 103mW, or 94% of threshold and a 4.5mW local oscillator.

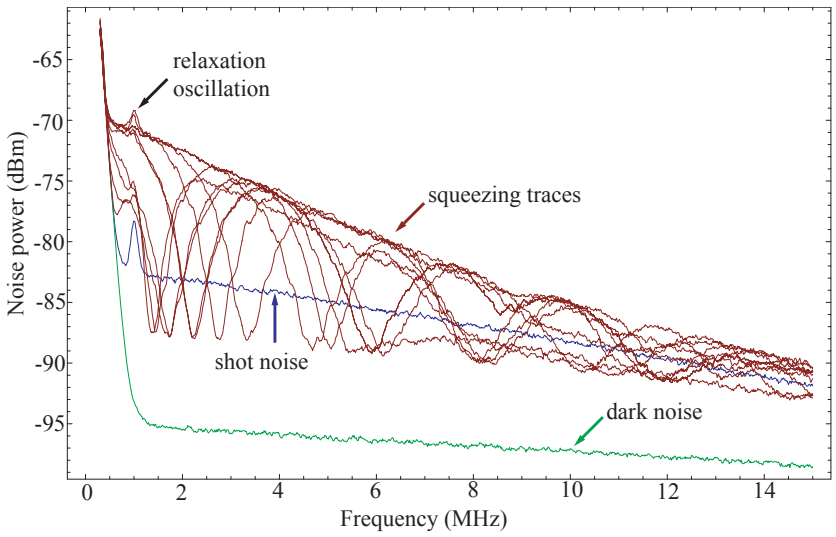

Figure 7.1: 15MHz span of PPKTP squeezing. The noise eater on the laser was turned off to show the position of the relaxation oscillation of the laser. Shot noise is shown by the blue trace, squeezing is indicated by the red and dark noise by the green, which was not subtracted from the data.

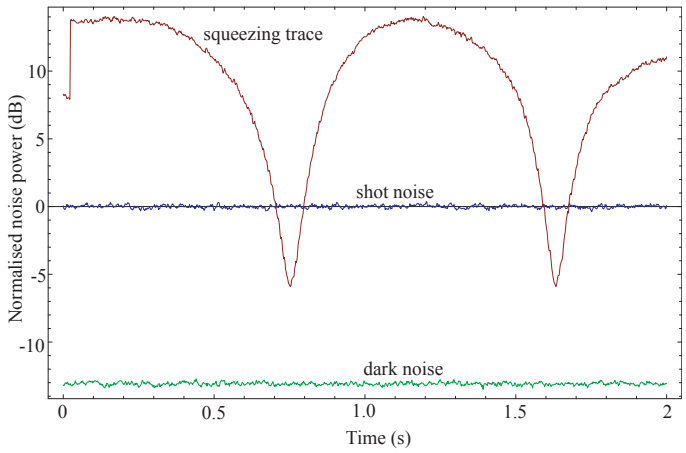

Figure 7.2: 0 span at 1.9MHz PPKTP squeezing with 2 second sweep time showing 5.8±0.1dB reduction in noise below the shot noise. Shot noise is shown by the blue trace, squeezing is indicated by the red and dark noise by the green, which was not subtracted from the data.

7.4.2 PPSLT

Figures 7.3 and 7.4 show the results for the PPSLT crystal. The threshold power for the OPO with this crystal was approximately 695mW. In figure 7.4 the green trace shows the squeezing obtained with a pump power of 470mW or 68% of threshold. 4.8±0.1dB of squeezing was observed with this input power. The red trace, however, shows the squeezing with an input power of 650mW or 94% of threshold. 4.9±0.1dB of squeezing was directly observed on this trace. A local oscillator power of 4.5mW was used for all traces.

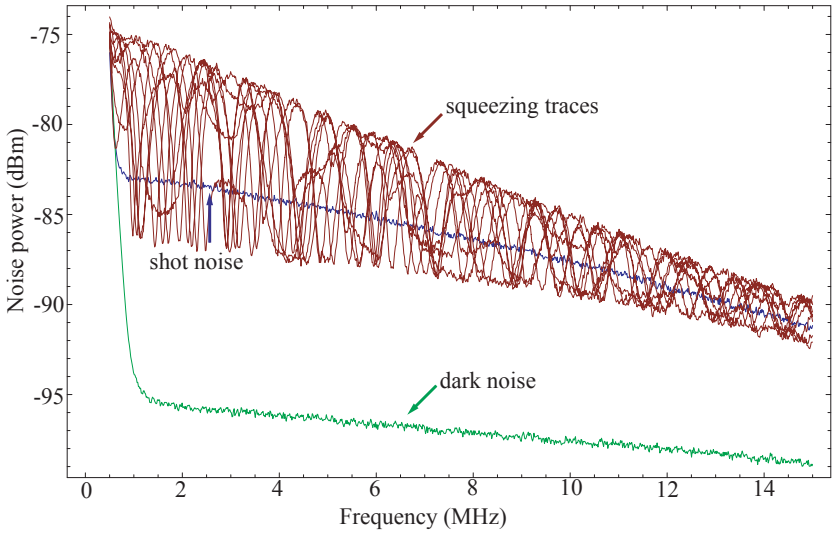

Figure 7.3: 15MHz span of PPSLT squeezing. Shot noise is shown by the blue trace, squeezing is indicated by the red and dark noise by the green, which was not subtracted from the data.

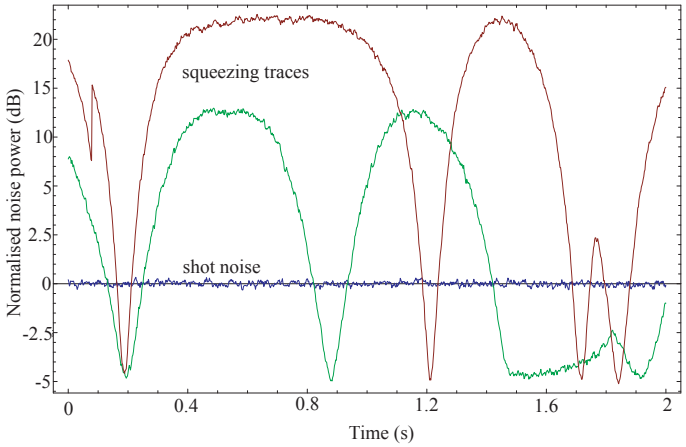

Figure 7.4: 0 span at 2.2MHz PPSLT squeezing with 2 second sweep time showing a maximum of 4.9±0.1dB reduction in noise below the shot noise. Shot noise is shown by the blue trace, squeezing with an input power of 470mW is indicated by the green trace and squeezing with an input pump power of 650mw is shown by the red trace. Dark noise was 13.6 ±0.1 dB below the shot noise but is not shown to emphasise the squeezing trace, and is not subtracted from the data.

7.4.3 MgO:PPSLN

Figures 7.5 and 7.6 show the squeezing obtained with MgO:PPSLN. The threshold was virtually impossible to measure for reasons which shall be discussed in the following chapter. At 1.7MHz 1.1±0.2dB of squeezing was directly observed with local oscillator of 4.5mW.

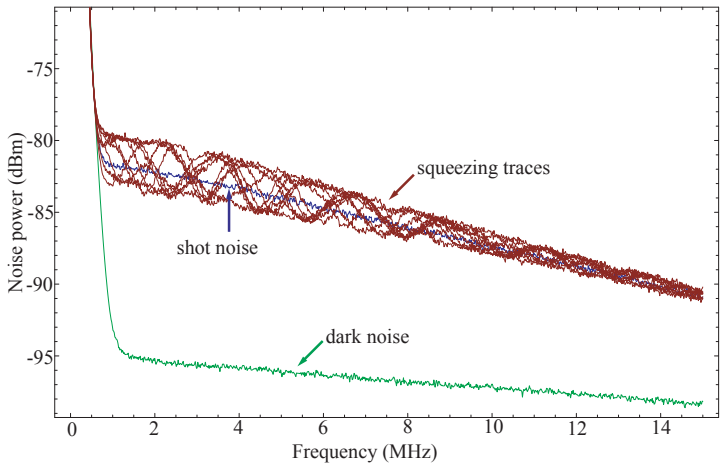

Figure 7.5: 15MHz span of PPSLN squeezing. Shot noise is shown by the blue trace, squeezing is indicated by the red and dark noise by the green, which was not subtracted from the data.

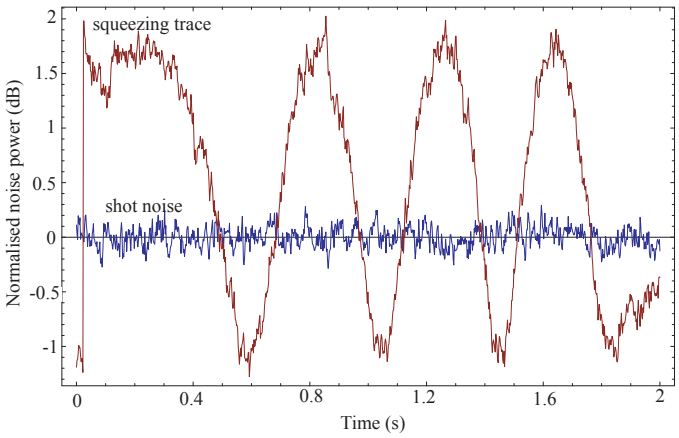

Figure 7.6: 0 span at 2.2MHz PPSLN squeezing with 2 second sweep time showing 1.1±0.2dB reduction in noise below the shot noise. Shot noise is shown by the blue trace and squeezing is indicated by both the red and green traces. The green trace corresponds to an input pump power of 470mW and the red trace corresponds to an input power of 650mW. Dark noise was 13.6 ±0.1 dB below the shot noise but is not shown to emphasise the squeezing trace, and is not subtracted from the data.

7.5 Inferred squeezing

From the traces it is possible to infer the squeezing and losses on the squeezed beam of our system. We do this by modelling the state exiting the cavity as a pure squeezed state, this means that the squeezed state is a minimum uncertainty state and hence we can write

$$V_{in}^{+} = \frac{1}{V_{in}^{-}} \tag{7.2}$$

where the subscript $_{in}$ is used to denote the squeezed beam leaving the cavity and about to enter external losses, which shall be modelled as a beamsplitter. By modelling the loss as a beamsplitter, we may write the variance of the squeezed beam for the amplitude and phase quadratures after the loss as

$$V_{out}^{\pm} = \eta(V_{in}^{\pm} - 1) + 1 \tag{7.3}$$

Where η is the transmissivity of the beam splitter chosen to represent loss on the squeezed beam. Solving this equation for both the amplitude and the phase quadrature will yield an estimate of the squeezing before losses and will also provide an estimate of the losses outside of the cavity.

For the PPKTP trace shown in figure 7.2, we find an inferred squeezing of 14dB and a loss on the squeezed beam of 24%. For the PPSLT trace shown in figure 7.4, we find an inferred squeezing of 9dB for the green trace which had a pump power of 470mW with a loss in the squeezing of 24% and for the red trace an inferred squeezing of 15dB is found with a loss of 30%.

7.6 Correcting for dark noise

Provided that the photocurrent noise from the local oscillator is much larger than the dark noise due to the electronic circuitry, it is valid to remove the dark noise from the traces of the shot noise and the squeezing which were obtained. This is done through subtraction of the noise power in dBm and can explicitly be written [9]

$$x' = 10Log_{10}\left(10^{\frac{x}{10}} - 10^{\frac{y}{10}}\right) \tag{7.4}$$

where x and x' are the values for shot noise or squeezing before and after dark noise correction in dBm, respectively, and y is the value of the dark noise in dBm. Table 7.1 shows the observed and calculated squeezing results obtained in this chapter. Inferred squeezing was not calculated for the MgO:PPSLN because the effect which was seen to reduce the squeezing, explored in the following chapter, does not allow for any comparisons to be made.

7.7 Summary

In this section we have described the procedures used to take our squeezing traces. Emphasis was made on the techniques used to create similar system parameters for all of the nonlinear materials. Squeezing traces were obtained which showed observed squeezing levels of 5.8±0.1dB for PPKTP, 4.9±0.1dB for PPSLT and 1.1±0.2dB for MgO:PPSLN. The threshold for PPKTP was found to be approximately 110mW and the threshold for PPSLT was 695mW. In the next chapter these results are analysed and we investigate the effects seen which may have reduced the observed squeezing. The subtraction of electronic noise, and squeezing inferred without detection loss, show that losses in the detection of the squeezed state was limiting the levels of squeezing which were observed.

	PPKTP	PPSLT	MgO:PPSLN
Maximum squeezing (dB below SNL)	5.8 ±0.1	4.9±0.1	1.1±0.2
Theoretical max squeezing from squeezing and anti-squeezing relationship (dB below QNL)	15 ±1	22 ±1	—
Shot noise power (dBm)	-82.1 ±0.1	-82.2 ±0.1	-82.9 ±0.2
Dark noise power (dBm)	-95.2 ±0.1	-95.8 ±0.1	-95.1 ±0.1
Maximum squeezing corrected for dark noise (dB below SNL)	6.5 ±0.1	5.4 ±0.1	—

Table 7.1: Observed and calculated squeezing results.

Analysis of Results

8.1 Poor squeezing from MgO:PPSLN

The poor squeezing results obtained with the MgO:PPSLN were due to an unexpected effect which we aim to quantify in this section. It was found that the reflectivity of the crystal would change with temperature in a periodic fashion. This was noticed by blocking the local oscillator and observing the power in one of the homodyne detectors, whilst at the same time, observing the power that passed through the cavity in the transmitted reverse direction seed photodetector. The forward seed was directed into the cavity whilst the reverse direction seed, the pump and the local oscillator were blocked. It was seen that at fairly regular intervals, the power in the transmitted forward direction would decrease around the point of maximum resonance as the cavity length was scanned. At the same time, the power in the reverse direction would increase. The cavity response of the forward direction seed at a temperature of $52.18°C$, where the effect was at its strongest, is shown in figure 8.1. This was not believed to be a nonlinear effect, because of its periodicity and also because the power in the forward seed was only 4.5mW, only approximately 0.02% of which was entering the cavity through the highly reflective mirror serving as the input coupler.

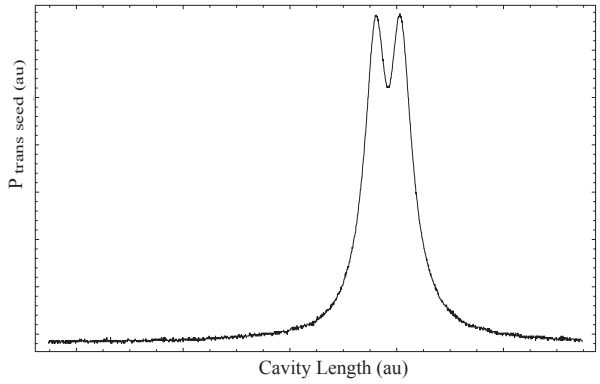

Figure 8.1: Output trace seen in one of the homodyne photodetectors with a forward direction seed entering the cavity. The length of the cavity is being scanned and we note that as resonance is approached, the forward direction power begins to drop at a certain point, the power in the reverse direction increases at this point.

To quantify this effect, the finesse of the cavity at a temperature with maximum reflectivity and at a temperature with minimum reflectivity was found. At $52.51°C$ there

was a minimum reflectivity and the finesse of the cavity was found to be 63. This was very high considering the finesse of the cavity without the crystal was 73, indicating that losses due to the crystal were low. Changing the temperature to $52.18°C$ would take us to an operating condition where maximum reflectivity would occur and the finesse of the cavity would drop to 35. This was due to the large amount of light which reflected off the surface of the cavity. Calculating the finesse of the cavity, it became apparent that the crystal was acting as a 4% reflector of the light. This amount of loss will destroy any hope of finding high levels of squeezing at the output as shown in figure 5.14. The loss of the crystal at the higher finesse is examined in the following section. From approximately $40°C$ to $70°C$ a similar effect was noticed across the entire range with a similar interval between minimum and maximum reflectivities.

It is believed that the material itself is very capable of producing high levels of squeezing, OPA gains of over 200 were observed, but with this effect present it would be necessary to find a phase matching condition which also was a minimum for this reflectivity effect and hope that the cavity dispersion would not put us far from the optimum. Such a condition could not be found, hence the poor squeezing results. This condition was most likely due to poor anti-reflection coatings creating an etalon out of the crystal, this is explored further in the following chapter.

8.2 Inferred losses

The finesse of the cavities for the three nonlinear materials was recorded in the hope of estimating the losses of the nonlinear materials. In the empty cavity, the finesse for 532nm was found to be 9.3 and the finesse for 1064nm was 73. The accuracy of these measurements are limited by the nonlinear response of the PZT. We only investigate the value for 1064nm as small losses will have a minor impact on the low finesse of the cavity at 532nm. Taking the three mirrors inside the bow-tie cavity which were not the input/output coupler for the pump to have a reflectivity of 0.999 at 1064nm, we find that the reflectivity of the input/output coupler must be 0.961 to give a finesse of 73 for the empty cavity. With these values it is then possible to determine the losses for each of the crystals and then infer the value of α_s, the absorption coefficient, given in equation 5.21. For the MgO:PPSLN these calculations were done for a temperature where the reflectivity of the crystal due to the temperature effect was at a minimum. If the MgO:PPSLN was indeed acting as an etalon, then the loss calculated for this material may be slightly lower than its true value because the etalon may set up a condition where virtually no light is reflected if the loss on both surfaces is equal. This would imply that loss from anti-reflection coatings which should be present on the material may not be taken into account. Equations 5.20 and 5.21 yield the results that the losses introduced by the three crystals are 0.9% for PPKTP and PPSLT and 0.5% for MgO:PPSLN. Assuming that the loss at the anti-reflection coatings for any of the crystals is $0.1\%\text{cm}^{-1}$, reveals that the absorption coefficients for each of the materials is $0.7\%\text{cm}^{-1}$ for the PPKTP and the PPSLT, and is $0.3\%\text{cm}^{-1}$ for the MgO:PPSLN. This shows that the losses in PPSLT and PPKTP were very similar, but the loss in the MgO:PPSLN may be approximately half the value of the other two crystals. Even if there is very little loss at the surface of the crystal due to a possible etalon effect, it still looks to be the case that losses due to internal absorption and scattering from the MgO:PPSLN is lower than the other two crystals, on account of the large differences between the values found for the three crystals.

8.3 Threshold and thermal effects

The difference between the threshold powers for the PPSLT and the PPKTP was an anomaly which deserves some attention. The very small variation in the two calculated nonlinear coupling coefficients of PPKTP and PPSLT, 2312 $s^{\frac{1}{2}}$ and 2394 $s^{\frac{1}{2}}$ respectively, indicate that threshold for the PPSLT should have occurred slightly before the value found for PPKTP . The threshold power for PPKTP was found to be 110mW and for PPSLT, approximately 695mW. One might then expect that high losses within the PPSLT were the reason for the high threshold value. This, however, does not seem to be the case, as it was shown in the previous section that the finesse of the cavity with either the PPKTP or the PPSLT crystal in, were almost identical. There was also no major difference between the finesse of the two crystals at 532nm, both were found to have a finesse of approximately 9. The conclusion then is that it is most likely that the nonlinear coefficient of the PPSLT is lower than that for PPKTP.

We can see that the PPKTP follows predictions from chapter 5 quite well in that experiment agrees with theory as to where threshold will occur. This is shown in figure 8.2 where the star has been added to show which operating regime the cavity was in. This is further evidence that the nonlinear coupling coefficient of the PPKTP is correct and hence the coefficient for PPSLT is much lower than calculated.

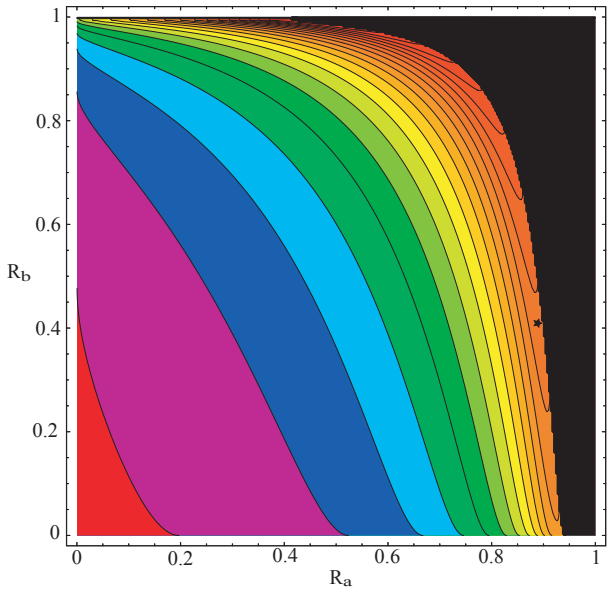

Figure 8.2: PPKTP OPO model with 110mW pump, which was the experimentally found threshold power for our setup. In the experiment the reflectivity of the input/output coupler was approximately 0.9 in the fundamental and 0.4 in the second harmonic. The model predicts that we are very close to threshold, agreeing with the experiment. At the star a squeezing level of 13.5dB is theoretically achievable, 5.8 ± 0.1dB was observed

Figure 8.2 shows that by choosing the input/output coupler reflectivities of the model to be equal to the values of the physical coupler and by setting an input power equal to the value for threshold found in the experiment of 110mW, the model predicts that we are close to threshold and that 13.5dB of squeezing may be found. In chapter 7 it was found that the experiment may have had an approximately 24% loss on the squeezed beam

outside of the cavity. For light which is squeezed at 13.5dB below the QNL, after a 24% loss we would expect to observe a squeezing level of 5.6dBṪhe model very closely predicts the value of squeezing which was observed in the experiment for the PPKTP.

To get an estimate of the nonlinear coupling coefficient of the PPSLT, we produce a plot similar to figure 8.2 which places the operating condition, noted by the star, right on threshold for an input power of 695mW. This plot is shown in figure 8.3 and it corresponds to a nonlinear coupling coefficient of 1000 $s^{-\frac{1}{2}}$, resulting in a estimate of the second order nonlinearity of $9.1pm/V$. This value indicates an estimate of the true value of the second order nonlinearity and has not been corrected for the first order phase matching. This value is much lower than the expected $13.8pm/V$ quoted in chapter 4, which was inferred from the congruent lithium tantalate.

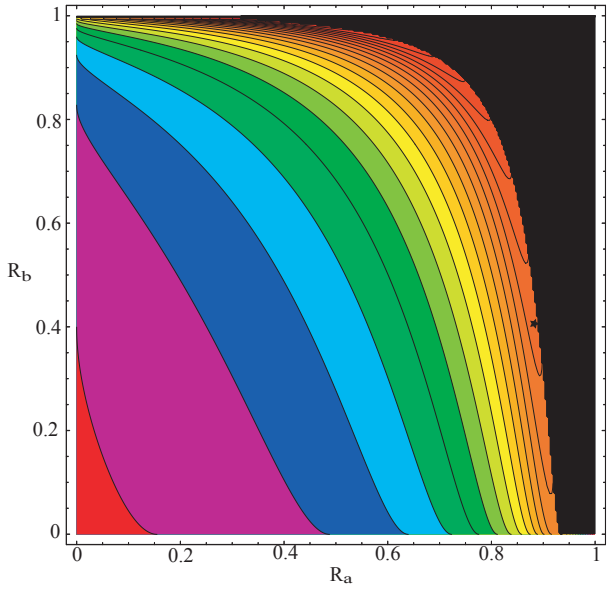

Figure 8.3: PPSLT OPO model with 695mW pump which was the threshold power for our experimental setup. The nonlinear coupling coefficient has been reduced from the previously calculated value of 2394 $s^{-\frac{1}{2}}$ to 1000 $s^{-\frac{1}{2}}$. At the star a squeezing level of 13.5dB is theoretically achievable, 4.9 ± 0.1dB was observed

The star in figure 8.3 denotes a theoretical squeezing of 13.5dB and with a loss of 24% on the squeezing we would expect to detect 5.6dB of squeezing. 4.8dB was observed which indicates that perhaps photothermal effects were increasing the loss of the system. Interestingly, the theoretical squeezing for both the PPKTP and the PPSLT is equal because the reduced squeezing expected due to the lower nonlinear coupling coefficient has been countered by increasing the pump power.

Raising the pump power has led to the introduction of many negative photothermal effects. It was seen in figure 7.6 that there was perhaps something limiting the ability of the apparatus to detect the squeezing. This was indicated by the growth of the anti-squeezing for higher powers whilst the squeezing did not improve. In chapter 7 it was also found that for the higher pump power, indicated by the trace with more anti-squeezing, the loss on the squeezed beam could be estimated at 30% as opposed to 24% on the lower power. The high powers needed to reach threshold with this crystal strongly degraded

the stability of the cavity lock. Once a lock was made and the pump became resonant, it would tend to drop lock very quickly, as the crystal may have began to heat at the waist. A difference in temperature between the middle and the outside of the crystal may have destabilised the cavity. It could take many attempts to get a cavity lock and once a lock was made it was also more prone to dropping. The fact that the lock was unstable may have affected the observable squeezing and could have accounted for the increase in detection losses due to phase jitter.

8.4 Wedged material

The wedge on the PPSLT crystal gave a definite advantage over the flat crystals. Whilst research has been undertaken into the use of a wedged material in standing-wave double-pass systems [30, 31], little to no experimental work has been done to investigate the effects of a wedged material in a travelling wave setup for an OPO or OPA, although its possible use has been noted [30]. In order to measure the usefulness of the wedge, the front seed and the pump were directed into the cavity and the reverse seed was blocked.

The length of the bow-tie cavity was scanned at 13Hz, whilst the phase of the pump was scanned at 500Hz. The Newport 3040 temperature controller was used to heat the crystal from $23°C$ to $40°C$. The change in temperature was nonlinear as the heating of the crystal at lower temperatures would occur more rapidly. Feeding the 4.5mW forward direction seed into the cavity, the intensity seen at the output of one of the detectors from the homodyne was viewed on a cathode ray oscilloscope. The dispersion due to the cavity reduces the maximum efficiency of amplification of the seed in much the same way that poor phase matching affected the outcome of SHG shown in figure 3.8. This effect, in the case of a DROPA, is explored by McKenzie *et al* [32], where it is shown that scanning the temperature of the crystal, resulting in a change in the phase matching condition, will result in a plot which shows the OPA gain sampling the the absolute value of a sinc function. For the wedged material this plot could be taken many times for differing crystal lengths by translating the nonlinear material. This would eventually lead to a maximum for the OPA gain as well as a plot for which the gains on either side of the optimum were similar in magnitude. The case of the optimised PPSLT is shown in figure 8.4 and the case of the unoptimised, flat PPKTP is shown in figure 8.5. It is important to note that the axes on the figures are in arbitrary units (au) because the intention of the figures is to only qualify the effect that the wedge has.

As expected, the PPSLT which has had the OPA gain maximised through translation of the crystal, has approximately equal gains on either side of the maximum. A possible absolute sinc fit has been added to illustrate this point, though it is important to note that the nonlinear response of the change in temperature will stretch the higher temperature end of the fit, and this is why a calculated fit was not added to the figure. Comparison with the flat PPKTP temperature run depicted in figure 8.5 shows that the dispersion caused by the cavity has moved the system from the optimum condition. This is indicated by the fact that there is no clear maximum gain with equal magnitude gains on either side, a possible fit to an absolute sinc shows where the optimum condition is likely to lie. To reach this optimum is no longer trivial as it was for the wedged material. For the flat PPKTP crystal, dispersion would have to be overcome by the introduction of a dispersion plate into the beam path within the cavity, which has been previously shown to provide positive results [33]. The dispersion plate, however, will introduce additional intra-cavity losses, shown in chapter 5 to drastically reduce the expected squeezing, and may also

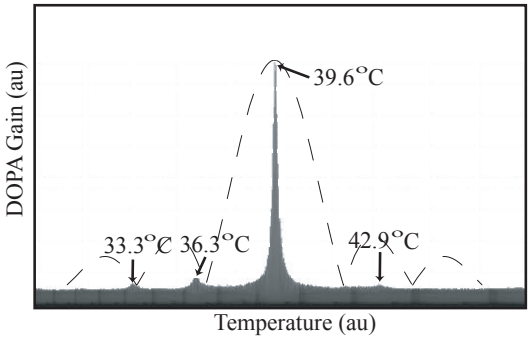

Figure 8.4: Temperature run of PPSLT showing seed gain with 430mW of pump power. A possible absolute sinc function envelope has been added.

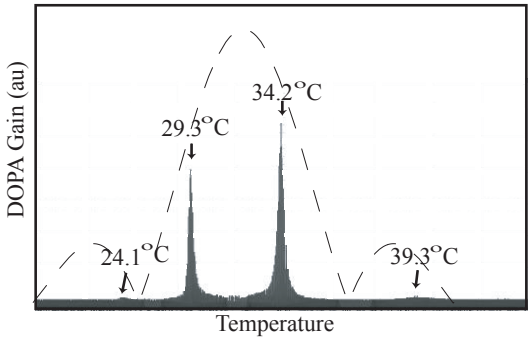

Figure 8.5: Temperature run of PPKTP showing seed gain with 84mW of pump power. A possible absolute sinc function envelope has been added.

misalign the cavity. The wedge does not introduce additional losses, as the light already had to pass through both faces of the crystal, and the wedge was not seen to introduce any misalignment of the cavity. The wedge on the quasi-phase matched material allowed for the gain to be optimised by accounting for dispersion caused by the cavity and had no discernible negative effects.

Conclusions and implications/future work

The aim of this experiment was to construct three squeezers with different nonlinear materials, in order to investigate the suitability of the materials for future sources of squeezed light. Towards this end, a model was constructed which was used to investigate many of the properties of the three squeezers and show the effect of various system parameters on the expected squeezing results, such as the reflectivity of the input/output coupler, intra-cavity loss and input pump power. To experimentally investigate the materials, an OPO was constructed using a bow-tie cavity. The bow-tie cavity allowed for the simple replacement of the nonlinear crystals, with minor effect to the rest of the experiment. This allowed for the characterisation of the three nonlinear crystals used, PPKTP, PPSLT and MgO:PPSLN, in what was essentially the same setup for all materials. Table 9.1 shows the important theoretical and experimentally observed values for all three materials.

	PPKTP	PPSLT	MgO:PPSLN
Maximum squeezing (dB below SNL)	5.8 ±0.1	4.9±0.1	1.1±0.2
Maximum squeezing corrected for dark noise (dB below SNL)	6.5 ±0.1	5.4 ±0.1	—
Theoretical max squeezing from squeezing and anti-squeezing relationship (dB below QNL)	15 ±1	22 ±1	—
Power at max squeezing (mW)	103	650	470
Inferred total loss from cavity finesse readings (cm^{-1})	0.7%	0.7%	0.3%
Threshold (mW)	110	695	—
Phase matching temp ($^{\circ}C$)	33.78	39.63	—

Table 9.1: Summary of important theoretical and experimental values. A reasonable estimate of threshold power and phase matching temperature for the MgO:PPSLN was not found due to the effect discussed in section 8.1.

9.1 Effects and properties that affected squeezing

- The effect which was most detrimental to the squeezing was that seen with the MgO:PPSLN. The intra-cavity loss of 4% at 1064nm, which this effect resulted in when it was at its worst, was the reason that only very low levels of squeezing were observed with MgO:PPSLN.

- The wedged PPSLT was able to produce much stronger suppression in the shot noise

of 4.9±0.1dB below the QNL. The wedge on this material certainly aided in the high level of squeezing which was observed, through compensation of the dispersion caused by the cavity. The wedge was seen to have no negative side-effects.

- The squeezing seen with the PPSLT, however, was not as high as might have been expected, because the threshold power was experimentally found to be 695mW, when a conservative estimate may have put threshold at approximately 150mW. This was seen to have most likely been due to a lower second order nonlinearity value than first expected. The estimated value was $13.8pm/V$, but experimentally this value was found to be closer to $9.1pm/V$.

- With a higher threshold power, photothermal effects became apparent for the PPSLT. The loss on the squeezed beam was estimated at 24% for both the PPKTP crystal and the PPSLT with pump powers of 470mW. Increasing the pump power to 650mW, however, showed an estimated detection loss of 30%, possibly due to phase-jitter. This highlighted the negative impact that photothermal effects may have on squeezing.

- PPKTP showed the highest directly observed levels of squeezing of 5.8±0.1dB. The fact that it fitted to the models very well indicates that the properties of the material were very close to the expected values. No negative effects were seen with the PPKTP.

- The total loss of the three crystals at 1064nm, due to the two anti-reflection coatings and internal losses, were found to be 0.9% for PPSLT and PPKTP, and 0.5% for MgO:PPSLN. This shows that in terms of losses, MgO:PPSLN has an advantage over the other two materials for the production of very strongly squeezed states, as explored in section 5.3.5.

9.2 Future directions

9.2.1 Reducing losses

The total losses on the squeezed beam, the lowest of which were estimated at 24%, were too high for the detection of very strongly squeezed states. In order to detect higher levels of squeezing, it would be necessary to reduce the losses that the squeezed beam experienced. The quantum efficiency of the ETX500 photodiodes used have recently been determined to be 95±2% [21]. The other major sources of loss are the visibility of the homodyne setup, the beamsplitter in the homodyne, and the two dichroic mirrors used to remove the pump beam from the squeezed light. Obviously, the losses on the beamsplitter could be minimised through improvement of the anti-reflection coating placed on it, in future experiments it would be wise to purchase a beamsplitter with the lowest expected losses. If we assume that we had a 10% loss from the two detectors, a 4% loss due to the low visibility of the setup, a 0.5% loss from the beamsplitter, then there is still a 9.5% loss on the squeezed beam, a fair proportion of which is expected to occur at the dichroic mirrors. The performance of dichroic mirrors is very sensitive to angle, so if one of the angles was not optimised this may have been a fairly large source of loss. It was deemed necessary to place two dichroic mirrors in the path of the squeezed beam because it was seen that a single dichroic mirror actually reflected a fairly large amount of 532nm light. A second dichroic was added so that an excess of 532nm light would not be present on

the photodetectors in the homodyne. Reduction on the loss due to these dichroic mirrors certainly needs to be addressed, in future experiments it would be advisable to characterise these mirrors, rather than trust the specification, and ensure that losses were kept at a minimum.

The visibility of the homodyne detector could also have been improved to further decrease the loss on the squeezed beam. Initially, there was an intention to place a small cavity in the path of the local oscillator to stabilise the beam, which was traveling over 4 metres from the laser to the homodyne detector. Problems were encountered with the particular cavity constructed which resulted in it being removed. It is expected that the insertion of a cavity into the path of the local oscillator may improve the visibility of the homodyne detector and this would certainly lead to higher observable levels of squeezing.

9.2.2 Model for MgO:PPSLN effect

The cause of the change in reflectivity, observed with the MgO:PPSLN crystal is worth investigating as it was a very serious effect which destroyed any hope of observing high levels of squeezing with this material. The periodicity of the effect indicates that perhaps the crystal was acting as a temperature sensitive etalon. This may have occurred due to a poor anti-reflection coating run or perhaps some defect on the crystal surface, causing the surfaces to act as reflectors. It would be desirable to construct a model which predicted the response of a bow-tie cavity with an etalon at its focus. Determining if the model was able to produce the cavity response seen in figure 8.1, would provide insight as to whether this was the cause of the effect.

9.2.3 Improving the squeezing model

The model created in chapter 5 was incredibly useful in determining methods for the enhancement of squeezing experiments. To improve this model it would be useful to add some indication on the plot as to where photorefractive damage or photothermal effects might begin to arise, such as a line which illustrated the point where the intra-cavity powers rose to above a certain threshold. For the region where photorefractive damage might occur, this value would differ for each crystal, but an investigation into the region where photothermal effects began to decrease the observed squeezing would most likely provide a more consistent value across the three materials and would almost certainly occur well before any damage to the crystals was seen.

9.2.4 Future sources of squeezing

The incredibly high threshold of the PPSLT would certainly put it at the bottom of the list when choosing a crystal to design a stable squeezing experiment. The PPKTP was able to reach threshold much quicker, most likely due to a higher second order nonlinear coefficient, which made for a more stable lock and hence higher levels of squeezing. Altering the input/output coupler reflectivities to increase the threshold power would increase the squeezing seen with the PPKTP as shown in the model produced in this thesis and it would still be possible to keep the threshold power down to a level where photothermal effects were not significant. The one advantage that the PPSLT crystal had, its wedge, was an incredibly beneficial modification, but this modification is not limited to PPSLT, any periodically poled material could theoretically have this feature added. Wedged crystals provide access to the full nonlinear interaction provided by the poled materials, with

no discernable negative effects. Unfortunately, a meaningful comparison cannot be made between the MgO:PPSLN and the PPKTP, except to say that the MgO:PPSLN was found to have a lower loss and theoretically a higher nonlinear coupling coefficient, which gives it an advantage over the other two materials. If the effect seen with this crystal were not present, then a wedged version of it would most likely be a strong contender along with wedged PPKTP for the best material to use for the future generation of stable, highly squeezed states.

Bibliography

[1] K. McKenzie, D. Shaddock, D. McClelland, B. Buchler, and P. Lam, "Experimental demonstration of a squeezing-enhanced power-recycled michelson interferometer for gravitational wave detetection," *Physical Review Letters*, vol. 88, no. 23, 2002.

[2] N. Treps, U. Andersen, B. Buchler, P. Lam, H.-A. Maître, Bachor, and C. Fabre, "Surpassing the standard quantum limit for optical imaging using nonclassical multimode light," *Physical Review Letters*, vol. 88, no. 22, 2002.

[3] M. Hillery, "Quantum cryptography with squeezed states," *Physical Review A*, vol. 61, 2000.

[4] J. Armstrong, N. Bloembergen, J. Ducuing, and P. Pershan, "Interactions between light waves in a nonlinear dielectric," *Physical Review Letters*, vol. 127, pp. 1918–1939, 1962.

[5] M. Yamada, N. Nada, and S. M., "First-order quasi-phase matched $LiNb0_3$ waveguide periodically poled by applying an external field for efficient blue second-harmonic generation," *Applied Physics Letters*, vol. 62, pp. 435–436, 1993.

[6] G. Miller, *Periodically Poled Lithium Niobate: Modeling, Fabrication, and Nonlinear-Optical Performance*. PhD thesis, Stanford University, 1998.

[7] D. Walls and G. Milburn, *Quantum Optics*. Springer-Verlag, 1995.

[8] B. Yurke, "Use of cavities in squeezed-state generation," *Physical Review A*, vol. 29, pp. 28–29, 1984.

[9] B. Buchler, *Electro-Optic Control of Quantum Measurements*. PhD thesis, Australian National University, 2001.

[10] D. Shaddock, *Advanced Interferometry for Gravitational Wave Detection*. PhD thesis, Australian National University, 1997.

[11] B. Saleh and M. Teich, *Fundamentals of photonics*. John Wiley And Sons, Inc., 1991.

[12] A. White, *Classical and Quantum Dynamics of Optical Frequency Conversion*. PhD thesis, Australian National University, 1997.

[13] G. Miller, R. Batchko, W. Tulloch, D. Weise, M. Fejer, and R. Byer, "42poled lithium niobate," *Optics Letters*, vol. 22, no. 24, pp. 1834–1836, 1997.

[14] K. McKenzie, N. Grosse, W. Bowen, S. Whitcomb, M. Gray, D. McClelland, and P. Lam, "Squeezing in the audio gravitational-wave detection band," *Physical Review Letters*, vol. 93, no. 16, 2004.

[15] M. Fejer, G. Magel, D. Jundt, and R. Byer, "Quasi-phase-matched second harmonic generation: Tuning and tolerances," *Journal of Quantum Electronics*, vol. 28, no. 11, pp. 2631–2654, 1992.

[16] S. Yoo, R. Bhat, C. Caneau, and M. Koza, "Quasi-phase-matched second-harmonic generation in AlGaAs waveguides with periodic domain inversion achieved by wafer-bonding," *Applied Physics Letters*.

[17] Y. Furukawa, K. Kitamura, A. Alexandrovski, R. R. K., M. M. Fejer, and G. Foulon, "Green-induced infrared absorption in mgo doped linb0_3," *Applied Physics Letter*, vol. 78, pp. 1970–1972, 2001.

[18] I. Shoji, T. Kondo, A. Kitamoto, M. Shirane, and R. Ito, "Absolute scale of second-order nonlinear-optical coefficients," *Journal of Optical Society of America B*, vol. 14, no. 9, pp. 2268–2294, 1997.

[19] R. Klein, G. Kugel, A. Maillard, K. Polgŕ, and A. Péter, "Absolute non-linear optical coefficients of LiNbo_3 for near stoichiometric crystal compositions," *Journal of optical materials*, vol. 22, pp. 171–174, 2003.

[20] "Oxide corporation products/services." World Wide Web electronic publication, 2006. http://www.opt-oxide.com/english, viewed October 2007.

[21] H. Vahlbruch, M. Mehmet, N. Lastzka, B. Hage, S. Chelkowski, A. Franzen, S. Goßler, K. Danzmann, and R. Schnabel, "Observation of squeezed light with 10db quantum noise reduction." 2007.

[22] T. Hatanaka, K. Nakamura, T. Taniuchi, H. Ito, Y. Furukawa, and K. Kitamura, "Quasi-phase-matched optical parametric oscillation with periodically poled stoichiometric LiTao_3," *Optics letters*, vol. 25, no. 9, pp. 651–653, 2000.

[23] S. Suzuki, H. Yonezawa, F. Kannari, M. Sasaki, and A. Furusawa, "7dB quadrature squeezing at 860 nm with periodically poled $KTiOPO_4$," *Applied Physics Letters*, vol. 89, 2006.

[24] C. Gardiner and M. Collett, "Input and output in damped quantum systems: Quantum stochastic differential equations and the master equation," *Physical Review A*, vol. 31, no. 6, pp. 3761–3768, 1985.

[25] P. Drummond, K. McNeil, and D. Walls, "Non-equilibrium transitions in sub/second harmonic generation I. Semiclassical theory," *Optica Acta*, vol. 27, pp. 321–335, 1980.

[26] G. Boyd and D. Kleinman, "Parametric interaction of focused gaussian light beams," *Journal of Applied Physics*, vol. 39, no. 8, pp. 3597–3639, 1968.

[27] Y. Chen and Y. Chen, "Analytical functions for the optimization of second-harmonic generation and parametric generation by focused gaussian beams," *Applied Physics B*, vol. 76, 2003.

[28] N. Grosse, "Private communication, bow-tie cavity design and equipment setup from harmonic entanglement experiment."

[29] H. Bachor and T. Ralph, *A Guide to Experiments in Quantum Optics*. WILEY-VCH Verlag GmbH & Co.KGaA, 2004.

[30] G. Imeshsev, M. Proctor, and M. Fejer, "Phase correction in double-pass quasi-phase-matched second-harmonic generation with a wedged crystal," *Optics Letters*, vol. 23, no. 3, pp. 165–167, 1998.

[31] I. Juwiler, A. Arie, A. Skliar, and G. Rosenman, "Efficient quasi-phase-matched frequency doubling with phase compensation by a wedged crystal in a standing-wave external cavity," *Optics Letters*, vol. 24, no. 17, pp. 1236–1238, 1999.

[32] K. McKenzie, M. Gray, P. Lam, and D. McClelland, "Nonlinear phase matching locking via optical readout," *Optics Express*, vol. 14, no. 23, pp. 11256–11264, 2006.

[33] S. Pearl, H. Lotem, and Y. Shimony, "Optimization of laser intracavity second-harmonic generation by a linear dispersion element," *Journal of the Optical Society of America*, vol. 16, no. 10, pp. 1705–1711, 1999.